Hindawi
Geofluids
Volume 2020, Article ID 8815729, 25 pages
https://doi.org/10.1155/2020/8815729

Research Article

Fluid Dynamics in a Thrust Fault Inferred from Petrology and Geochemistry of Calcite Veins: An Example from the Southern Pyrenees

Daniel Muñoz-López[1], **David Cruset**[2], **Irene Cantarero**[1], **Antonio Benedicto**[3], **Cédric M. John**[4] and **Anna Travé**[1]

[1]*Departament de Mineralogia, Petrologia i Geologia Aplicada, Facultat de Ciències de la Terra, Universitat de Barcelona (UB), Martí i Franquès s/n, 08028 Barcelona, Spain*
[2]*Group of Dynamics of the Lithosphere (GDL), Geosciences Barcelona, GEO3BCN-CSIC, Lluís Solé i Sabarís s/n, 08028 Barcelona, Spain*
[3]*UMR CNR GEOPS, Université Paris-Saclay, 91405 Orsay, France*
[4]*Department of Earth Science and Engineering, Imperial College London, London SW7 2BP, UK*

Correspondence should be addressed to Daniel Muñoz-López; munoz-lopez@ub.edu

Received 8 April 2020; Revised 10 August 2020; Accepted 2 September 2020; Published 25 September 2020

Academic Editor: Paul D. Bons

Petrographic and geochemical analyses ($\delta^{18}O$, $\delta^{13}C$, $^{87}Sr/^{86}Sr$, clumped isotopes, and elemental composition) coupled with field structural data of synkinematic calcite veins, fault rocks, and host rocks are used to reconstruct the episodic evolution of an outstanding exposed thrust zone in the Southern Pyrenees and to evaluate the fault behavior as a conduit or barrier to fluid migration. The selected thrust displaces the steeply dipping southern limb of the Sant Corneli-Bóixols anticline, juxtaposing a Cenomanian-Turonian carbonate unit against a Coniacian carbonate sequence. Successive deformation events are recorded by distinct fracture systems and related calcite veins, highlighting (i) an episodic evolution of the thrust zone, resulting from an upward migration of the fault tip (process zone development) before growth of the fault (thrust slip plane propagation), and (ii) compartmentalization of the thrust fault zone, leading to different structural and fluid flow histories in the footwall and hanging wall. Fractures within the footwall comprise three systematically oriented fracture sets (F1, F2, and F3), each sealed by a separate generation calcite cement, and a randomly oriented fracture system (mosaic to chaotic breccia), cemented by the same cements as fracture sets F1 and F2. The formation of fractures F1 and F2 and the mosaic to chaotic breccia is consistent with dilatant fracturing within the process zone (around the fault tip) during initial fault growth, whereas the formation of the latest fracture system points to hybrid shear-dilational failure during propagation of the fault. The continuous formation of different fracture systems and related calcite cementation phases evidences that the structural permeability in the footwall was transient and that the fluid pathways and regime evolved due to successive events of fracture opening and calcite cementation. Clumped isotopes evidence a progressive increase in precipitation temperatures from around 50°C to 117°C approximately, interpreted as burial increase linked to thrust sheet emplacement. During this period, the source of fluid changed from meteoric fluids to evolved meteoric fluids due to the water-rock interaction at increasing depths and temperatures. Contrary to the footwall, within the hanging wall, only randomly oriented fractures are recognized and the resulting crackle proto-breccia is sealed by a later and different calcite cement, which is also observed in the main fault plane and in the fault core. This cement precipitated from formation fluids, at around 95°C, that circulated along the fault core and in the hanging wall block, again supporting the interpretation of compartmentalization of the thrust structure. The integration of these data reveals that the studied thrust fault acted as a transverse barrier, dividing the thrust zone into two separate fluid compartments, and a longitudinal drain for migration of fluids. This study also highlights the similarity in deformation processes and mechanisms linked to the evolution of fault zones in compressional and extensional regimes involving carbonate rocks.

1. Introduction

The study of outcrop analogues in fractured carbonate reservoirs is important to better understand the characteristics and evolution of synkinematic fracture systems and their control on fluid migration during crustal deformation [1–4]. In areas undergoing compressional regimes, the largest fluid fluxes, mass transfer, and heat transport commonly occur along the main thrust faults and related fracture networks because of the loading induced by thrust sheet emplacement [5–7]. By contrast, fluid flow rates in adjacent rock-matrix and poorly connected synkinematic fractures are commonly very low and fluid composition are often rock-buffered [6, 8]. In some cases, the development of thrust systems may also inhibit vertical fluid transport inducing fluid overpressure [9–11] leading to hydraulic fracturing [12–14]. Whether a fault zone will constitute either a conduit or barrier to fluid migration depends, among other factors, on the architecture of the fault zone and the permeability associated with the developed structures [15, 16]. Since the fault zone consists of a fault core, which is usually formed of low-permeability fault rocks, and a damage zone, which mainly includes extensional fractures and faults, overall permeability of the fault is conditioned by the amount, the spatial distribution, and the internal composition of these two fault zone elements [15, 17]. Besides, such structural permeability is dynamic and may vary spatially and temporally across the fault zone due to successive episodes of fracture opening and cementation [18, 19].

Although numerous studies based primarily on structural and numerical data have provided conceptual and analytical models on the architecture, mechanical properties, and fluid flow along fault zones [7, 15, 20], there exist only a few studies coupling field data and geochemistry of synkinematic minerals filling fractures that characterize the fluid migration through a thrust zone [21–25] and its spatial behavior as a conduit or barrier system [26, 27]. An outstanding exposed thrust in the Southern Pyrenees was chosen as a case study to evaluate qualitatively the fault-related permeability and its control on the fluid flow within and around the fault zone. Here, we combine structural, petrological, and geochemical data of calcite veins and host rocks present in the studied thrust zone. Therefore, the main objectives of this paper are (i) to determine the origin, composition, and temperature of the vein-forming fluids and the timing of fluid migration in relation to the fracturing events and (ii) to discern the fluid pathways, the extent of fluid-rock interaction, and the transfer of fluids across a fault zone during thrusting. The field and lab results are then compared with other studies reporting fluid flow within fault zones in other geological settings to generalize our conclusions to fault zones in carbonate settings.

2. Geological Setting

The Pyrenees constitute an asymmetrical and doubly verging orogenic belt that resulted from the Alpine convergence between the Iberian and European plates from Late Cretaceous to Oligocene, causing the inversion of previous Mesozoic rift basins and their incorporation into the thrust system [28–32]. The Pyrenean structure consists of a central antiformal stack of basement-involved thrust sheets from the axial zone [30], flanked by two oppositely vergent fold-and-thrust belts and their related Cenozoic Aquitaine and Ebro foreland basins [30, 33] (Figure 1(a)).

The South Pyrenean fold-and-thrust belt comprises a piggy-back imbrication of south verging and east-west striking thrust sheets involving Mesozoic and Tertiary cover rocks detached above Late Triassic evaporites [34] and transported southwards over the Ebro foreland basin. From north to south, they are the Bóixols thrust sheet, emplaced during the Late Cretaceous to Paleocene, the Montsec thrust sheet, originated during the Paleocene to late Ypresian, and the Serres Marginals thrust sheet, formed during the Lutetian-Oligocene [35, 36] (Figure 1(a)). In the frontal part of the Bóixols thrust sheet, a south verging and east-west trending fault-related anticline developed in relation to the propagation of the Bóixols thrust (the Sant Corneli-Bóixols anticline; Figures 1(b) and 1(c)). It is characterized by a gently dipping northern backlimb and a vertical to overturned southern forelimb [37].

Rocks cropping out along the Bóixols anticline comprise a large stratigraphic record ranging in age from Jurassic to Oligocene and deposited during the main tectonic events that affected the study area [38] (Figures 1(b) and 2). The stratigraphic sequence includes prerift Jurassic limestones and dolostones, synrift Lower Cretaceous limestones, marls and clays, preorogenic (postrift) Late Cenomanian to Santonian limestones, sandy limestones and marls and synorogenic Late Santonian to Oligocene marls and clays, sandstones, sandy limestones, and conglomerates ([38] and references therein).

In the central part of this anticline, the southern tilted forelimb is offset by minor low-dipping south-directed thrusts developed after the main folding phase, as evidenced by the displacement of already folded beds [38–40]. Therefore, they have been interpreted as postfolding accommodation structures or as hanging wall splays of the main Bóixols thrust [39, 40, 42]. One of these minor thrust faults is well exposed 2 km southeast of the Bóixols village (15 km of the L511 road), in the southern-central Pyrenees (Figure 3), exhibiting a complex calcite-filled fracture network developed in the fault core and damage zone of both the footwall and hanging wall of this reverse fault. This outcrop represents an exceptional field analogue to observe in a 300 m long outcrop the variation in deformation mechanisms developed across a fault zone and its contribution as seal or conduit for fluids. In this area, the studied thrust juxtaposes the Upper Cretaceous Santa Fe Formation against the Collada Gassó Formation (Figures 2 and 3). The Collada Gassó Formation [43] is formed of Coniacian grainstones with the variable presence of quartz, marly limestones, and limestones with abundant fossil content and has a general thickness of 150 to 250 m [38]. The Santa Fe Formation [44] is basically constituted of Cenomanian-Turonian limestones with a general thickness of 20 m [38].

3. Methodology

This study combines field structural data, including bedding and fracture orientation and dips, fracture type identification,

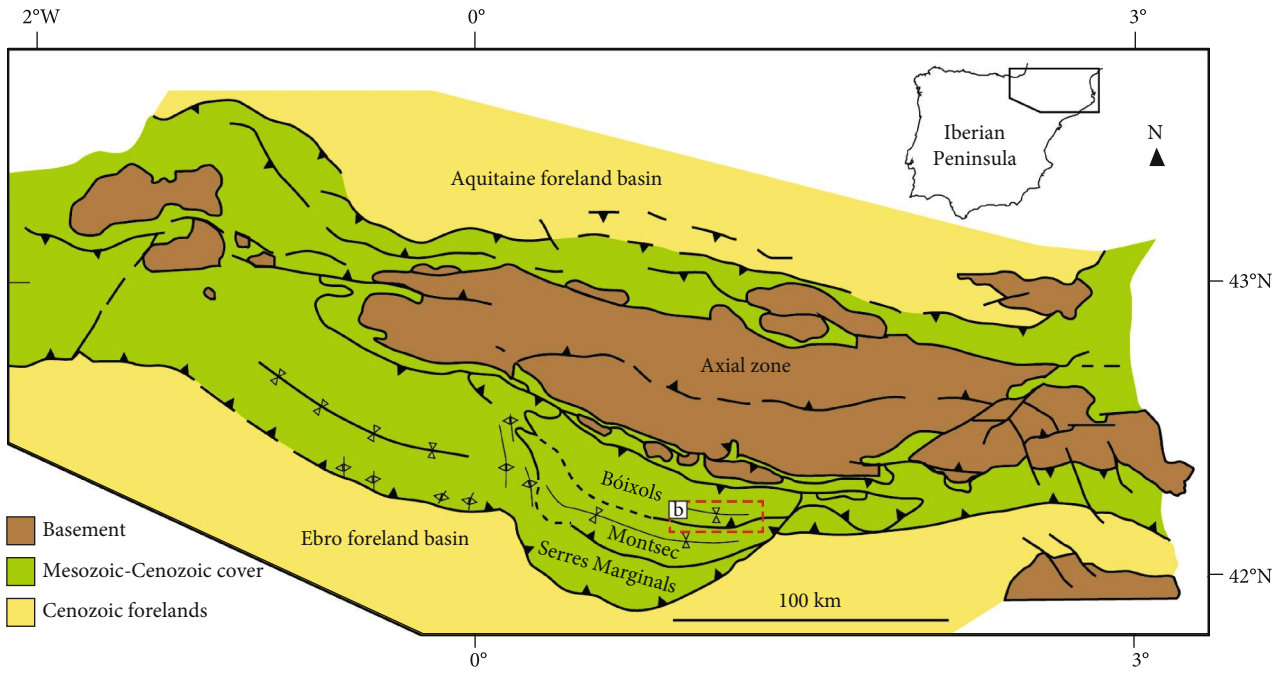

(a)

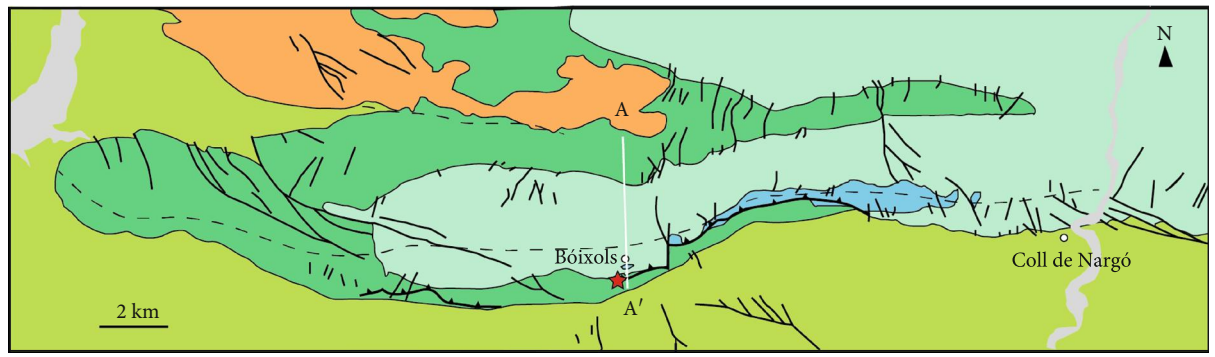

Village
Outcrop
Fold trace
Paleocene-Oligocene syn-orogenic sequence
Santonian-Eocene syn-orogenic sequence
Cenomanian-Santonian pre-orogenic (post-rift) sequence
Lower Cretaceous syn-rift sequence
Jurassic pre-rift sequence

(b)

Figure 1: Continued.

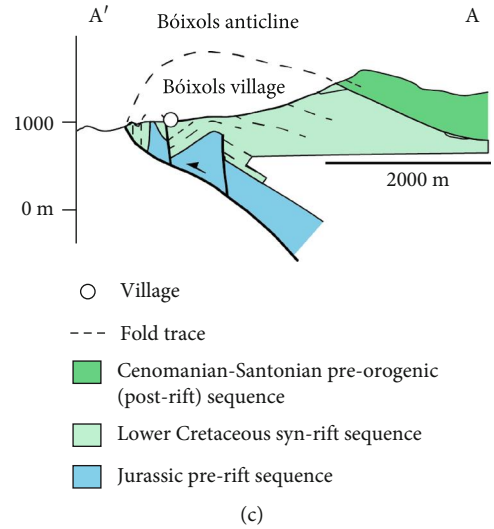

FIGURE 1: (a) Simplified geological map of the Pyrenees (modified from [32]). (b) Geological map of the Sant Corneli-Bóixols anticline showing the studied outcrop (modified from [38, 39]). (c) N-S cross section of the Sant Corneli-Bóixols anticline (modified from [40]). Location is shown in (b).

kinematics, and crosscutting relationships, with petrological and geochemical analyses. Structural data were plotted in equal-area lower-hemisphere projections, and different fracture sets were established according to their type, strike, orientation respect to bedding, mineral infillings, and relative age deduced from crosscutting relationships. Representative samples of each fracture generation and related host rocks were sampled in order to perform petrological and geochemical analyses. Thin sections were prepared and studied under optical and cathodoluminescence microscopes at the Facultat de Ciències de la Terra of the Universitat de Barcelona, using a Zeiss Axiophot optical microscope and a Technosyn Cold Cathodoluminescence microscope, model 8200 Mk5-1 operating between 16–19 kV and 350 μA gun current.

Thirty-one samples of calcite cements and host rocks were sampled for carbon and oxygen isotopic analysis using a 500 μm-diameter dental drill. Around 50-100 μg of each sample was reacted with 100% phosphoric acid for two minutes at 70°C. The resultant CO_2 was analyzed with an automated Kiel Carbonate Device attached to a Thermal Ionization Mass Spectrometer Thermo Electron MAT-252 (Thermo Fisher Scientific) following the method of [45]. The International Standard NBS-18 and the internal standard RC-1, traceable to the International Standard NBS-19, were used for calibration. The standard deviation is ±0.03‰ for $\delta^{13}C$ and ±0.05‰ for $\delta^{18}O$ expressed with respect to the VPDB standard (Vienna Pee Dee Belemnite). Analyses were carried out at "Centre Científics i Tecnològics" of the Universitat de Barcelona (CCiTUB).

The elemental composition of the calcite cements and related host rocks (12 samples in total) was analyzed with a high-resolution inductively coupled plasma-mass spectrometer (HR-ICP-MS, model Element XR, Thermo Fisher Scientific). Around 100 mg of each sample was extracted with a 400/500 μm-diameter dental drill, and then, powdered samples were dried at 40°C for 24 h. Then, 100 mg of sample was acid digested in closed polytetrafluoroethylene (PTFE) vessels with a combination of $HNO_3 + HF + HClO_4$ (2.5 mL : 5 mL : 2.5 mL *v*/*v*). The samples were evaporated, and 1 mL of HNO_3 was added to make a double evaporation. Finally, the samples were redissolved and diluted with Milli-Q water (18.2 MΩ cm^{-1}) and 1 mL of HNO_3 in a 100 mL volume flask. In order to improve the sensitivity of the ICP-MS, a tuning solution containing 1 g L^{-1} Li, B, Na, K, Sc, Fe, Co, Cu, Ga, Y, Rh, In, Ba, Tl, and U was used, and as internal standard, 20 mg L^{-1} of a monoelemental solution of ^{115}In was used. Reference materials are the BCS-CRM no. 393 (ECRM 752-1) limestone, JA-2 andesite, and JB-3 basalt. The precision of the results was expressed in terms of two standard deviations of a set of eight reference material measurements (reference material JA-2), whereas accuracy (%) was calculated using the absolute value of the difference between the measured values obtained during the analysis and the certified values of a set of eight reference material analysis (reference material BCS-CRM no. 393 for major oxides and JA-2 for trace elements). The detection limit (DL) was calculated as three times the standard deviation of the average of ten blanks. Analyses were performed at the Geochemistry Facility of labGEOTOP of Geoscience Barcelona (GEO3BCN-CSIC).

The $^{87}Sr/^{86}Sr$ isotope ratios were analyzed in calcite cements and host rocks (9 samples). Powdered samples were fully dissolved in 5 mL of 10% acetic acid. After centrifugation, the supernatant was dried and dissolved in 1 mL of 1 M HNO_3. The resulted solid residue, generated after evaporation, was diluted in 3 mL of 3 M HNO_3 and loaded into chromatographic columns to separate the Rb-free Sr fraction, by using SrResin™ (crown-ether (4,4′(5′)-di-t-butylcyclohexano-18-crown-6)) and 0.05 M HNO_3 as eluent. After evaporation, samples were loaded onto a Re filament along with 1 μL of 1 M phosphoric acid and 2 μL of Ta_2O_5. Isotopic ratio analyses were carried out in a TIMS-Phoenix mass

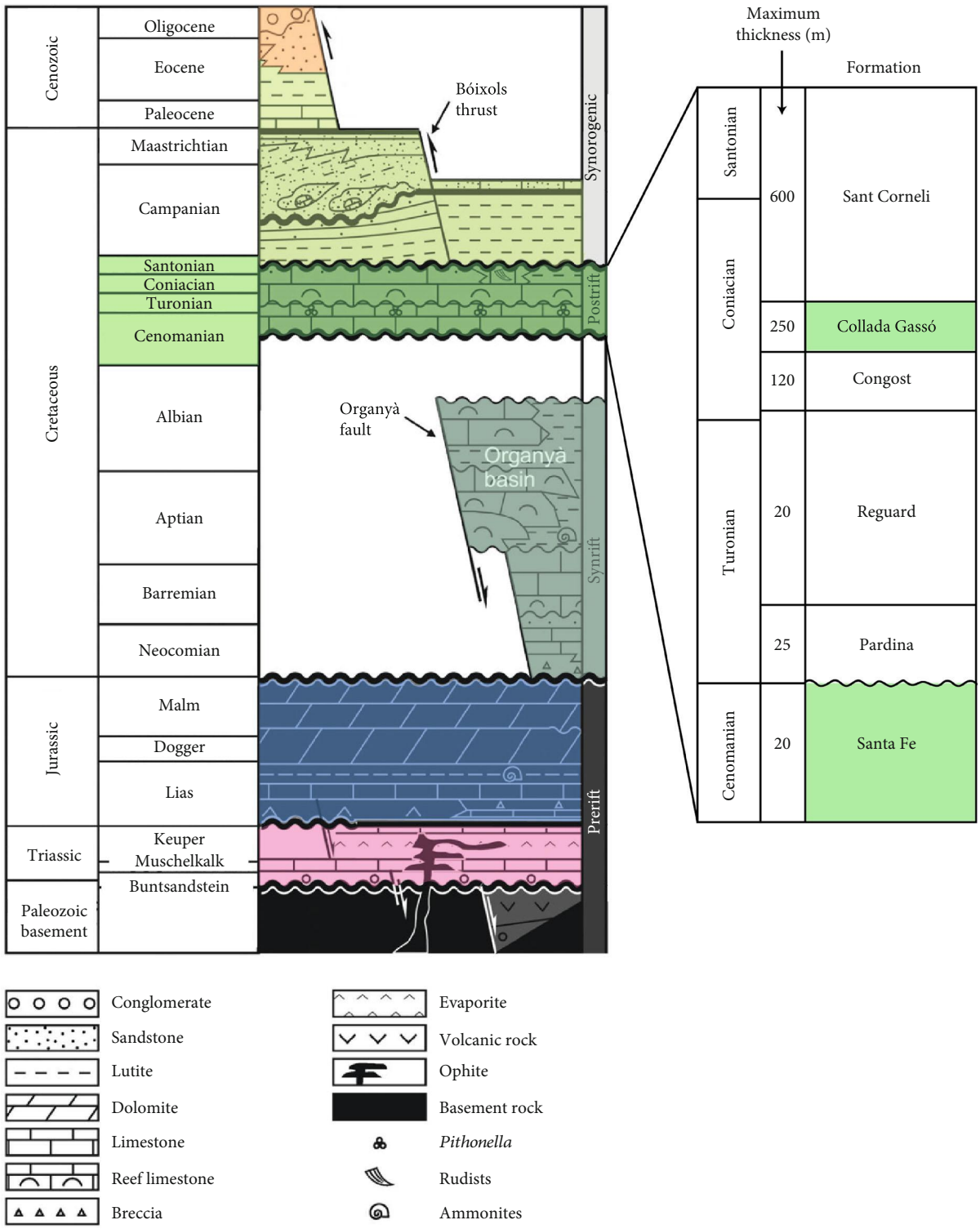

Figure 2: Chronostratigraphic diagram showing the main stratigraphic sequences and their related tectonic event [41]. The preorogenic (postrift) sequence, where the thrust was emplaced, is colored in green. The right panel shows a detail of the formations forming this sequence. Thickness and age of these formations are based on [38].

spectrometer (Isotopx) following a dynamic multicollection method, during 10 blocks of 16 cycles each one, maintaining a ^{88}Sr beam intensity of 3-V. Isotopic ratios were corrected for ^{87}Rb interferences and normalized using the reference value of $^{88}Sr/^{86}Sr = 0.1194$, in order to correct for the possible mass fractionation during loading and analysis of the sample. During sample analysis, the isotopic standard NBS-987 was analyzed six times, yielding an average value of 0.710243 ±

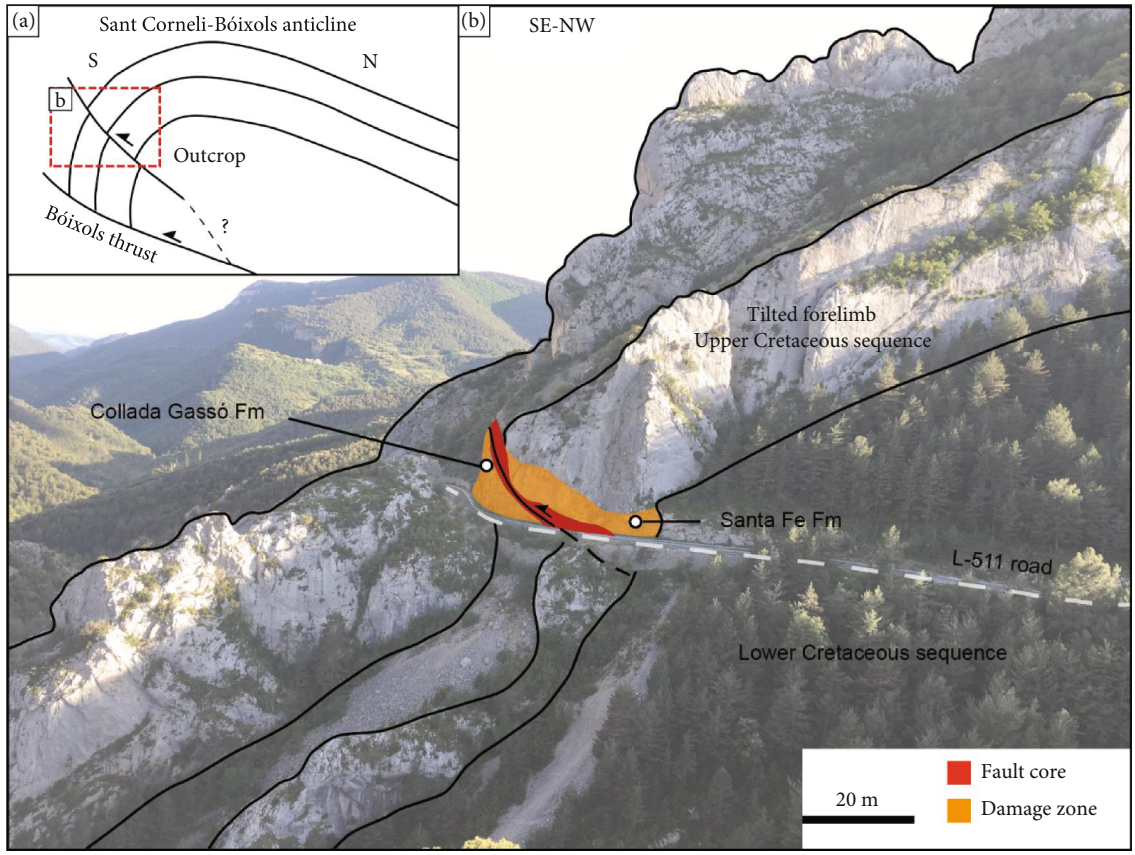

Figure 3: (a) Sketch and (b) panoramic view of the studied thrust offsetting the southern limb of the Sant Corneli-Bóixols anticline.

0.000009 (standard deviation, 2σ). NBS 987 data have been used to correct the sample ratios for standard drift from the certified value. The analytical error in the $^{87}Sr/^{86}Sr$ ratio, referred to two standard deviations, was 0.01%, whilst the internal precision is 0.000003. Sr procedural blanks were always below 0.5 ng. Analyses were carried out at the "CAI de Geocronología y Geoquímica Isotópica" of the Universidad Complutense de Madrid.

The $^{143}Nd/^{144}Nd$ isotope ratios were also analyzed in calcite cements and host rocks (9 samples in total). Samples were weighed in Teflon® vessels, with enriched spike solution (^{149}Sm-^{150}Nd, Oak Ridge) and dissolved in 5 mL of ultrapure HF and 3 mL of ultrapure HNO_3 (Merck-Suprapur™). The PFA vessels were placed for 65 hours into an oven at 120°C. Then, cold vials were evaporated on a heat plate at 120°C. 4 mL of distilled 6N HCl was added to the dried samples and placed in an oven overnight at 120°C. The resulted solid residue, generated after evaporation, was dissolved in 3 mL of distilled and titrated 2.5N HCl. In order to separate the dissolved fraction from the residue, if any, samples were centrifuged for 10 minutes at 4000 rpm. Chromatographic separation of the total group of REE was performed using cation exchange resin DOWEX 50W-X8 200-400 mesh (previously calibrated). Then, recovered REE fractions were completely dried and again dissolved in 200 μL 0.18N HCl. These solutions were passed in a new chromatographic step (Ln-resin) in order to obtain a complete separation between the Nd and the Sm fractions (using 0.3N HCl and 0.4N HCl as eluent, respectively). Dried Sm and Nd samples dissolved with 2 μL of 0.05 M phosphoric acid were loaded onto a side rhenium (Re) filament of a triple Re filament arrangement. Nd ratios were analyzed in a mass spectrometer TIMS-Phoenix®, following a dynamic multicollection method, through 160 cycles at a stable intensity of 1 V for the ^{144}Nd mass. In turn, Sm ratios were analyzed in the same spectrometer, following a single static method through 112 cycles maintaining 1 V intensity for the ^{149}Sm mass. Nd measurements were corrected for possible ^{142}Ce and ^{144}Sm interferences and they were normalized to a constant ratio of $^{146}Nd/^{144}Nd = 0.7219$ to correct the possible mass fractionation during the processes of loading and analyzing at the TIMS. Nd isotopic standard JNdi-1 was checked along with the samples to correct the sample ratios for standard drift from the certified value. The analytical error (2STD) in the $^{147}Sm/^{144}Nd$ ratio was 0.1% and in the $^{143}Nd/^{144}Nd$ ratio was 0.006%. Procedural blanks were always below 0.1 ng. Analyses were performed at the "CAI de Geocronología y Geoquímica Isotópica" of the Universidad Complutense de Madrid.

Clumped isotope thermometry was applied to four representative samples of the calcite cements Cc1 to Cc4 in order to determine the temperature and $\delta^{18}O_{fluid}$ in ‰VSMOW of the vein-forming fluids. Around 2–3 mg aliquots of powdered calcite cements was measured with an automated line developed at Imperial College London (the Imperial Batch Extraction system, IBEX). Samples were dropped in 105%

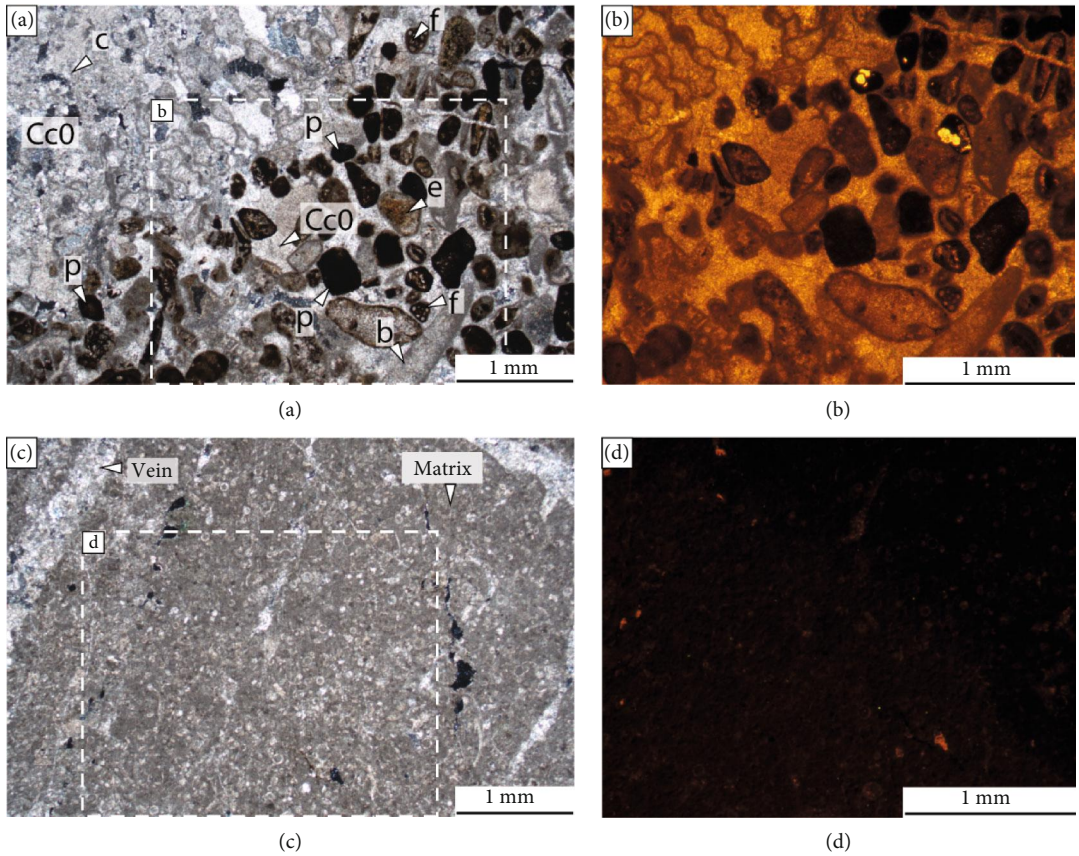

Figure 4: (a, b) Plane-polarized light and cathodoluminescence microphotographs of the footwall host rocks consisting of a grainstone made up of corals (c), foraminifers (f), bivalves (b), echinoids (e), and peloids (p), cemented by calcite (Cc0). (c, d) Plane-polarized light and cathodoluminescence microphotographs of the hanging wall host rocks composed of a wackestone of calcispheres and planktonic foraminifera.

phosphoric acid at 90°C and reacted for 30 minutes. The reactant CO_2 was separated with a Poropak Q column and transferred into the bellows of a Thermo Scientific MAT 253 mass spectrometer. The characterization of a single replicate consisted of 8 acquisitions in dual inlet mode with 7 cycles per acquisition. The total time of analysis per replicate is ~2 hours, and each sample was replicated at least 3 times. The postacquisition processing was completed with software for clumped isotope analyses (Easotope) [46]. During phosphoric acid digestion, Δ_{47} values were corrected for isotope fractionation with a phosphoric acid correction of 0.069‰ at 90°C for calcite [47]. The data were also corrected for nonlinearity applying the heated gas method [48] and projected into the reference frame of [49]. Carbonate $\delta^{18}O$ values were calculated with the acid fractionation factors of [50]. Results were converted to temperatures applying the calibration method of [51]. Calculated $\delta^{18}O_{fluid}$ values are expressed in ‰ with respect to the Vienna Standard Mean Ocean Water (VSMOW).

4. Results

4.1. Nature of Host Rocks. In the study area, two Upper Cretaceous sequences are present [38, 42]: the Collada Gassó Formation, located in the footwall, and the Santa Fe Formation, located in the hanging wall.

The Collada Gassó Formation consists of massive to well-bedded dark grey to brown limestones with an E-W orientation and dipping 80° towards the north. The limestones consist of grainstones made up of bivalves, gastropods, echinoids, bryozoans, corals, miliolids, partially to totally micritized components (i.e., peloids), and locally quartz grains. The inter- and intraparticle porosity is cemented by calcite cement (Cc0) (Figure 4(a)). Under cathodoluminescence, the skeletal components show a dull to bright brown color, whereas the inter- and intraparticle calcite cement (Cc0) displays a bright yellow color (Figure 4(b)). This formation is characterized by the widespread presence of bedding-parallel compaction stylolites, developed during progressive burial prior to deformation.

The Santa Fe Formation consists of a massive succession of grey limestones with an E-W orientation and dipping 80–85° towards the north. The limestones are made up of wackestones, locally packstones, with a notably presence of calcispheres and planktonic foraminifera (Figure 4(c)). Under cathodoluminescence, it exhibits a very dark orange color (Figure 4(d)).

4.2. Fault Zone Structure. The studied fault zone exhibits a classical fault organization with a main slip plane, a fault core, and two surrounding damage zones within the footwall and hanging wall, respectively (Figures 5 and 6). The slip plane

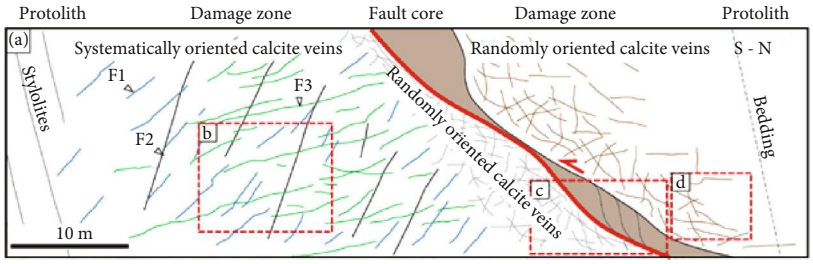

(a)

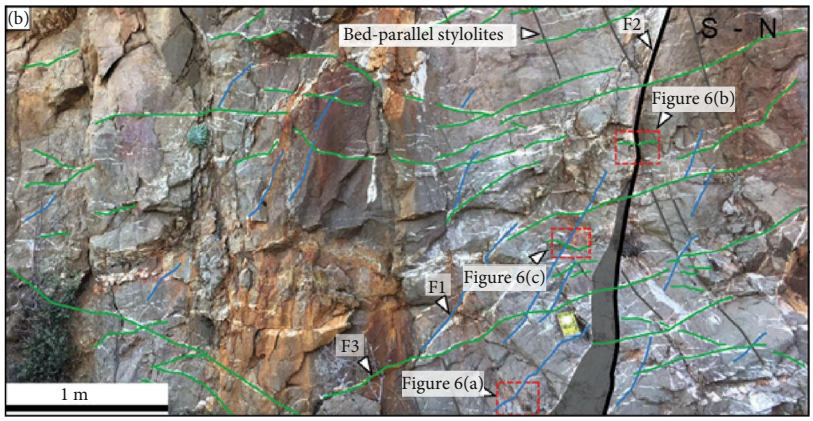

(b)

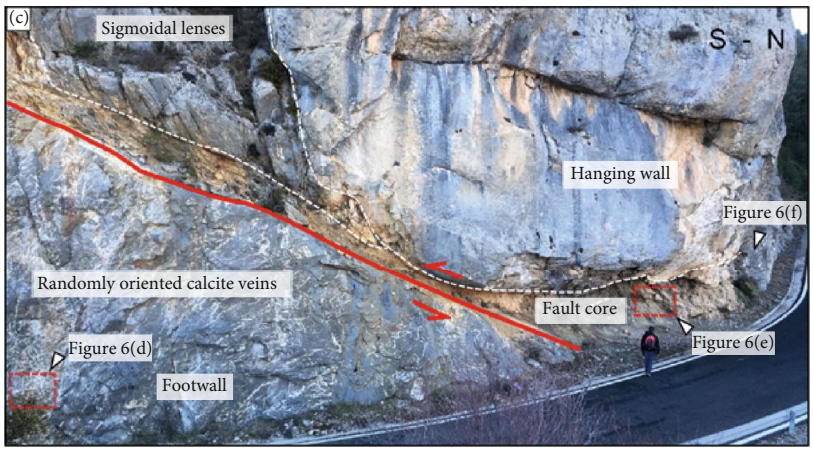

(c)

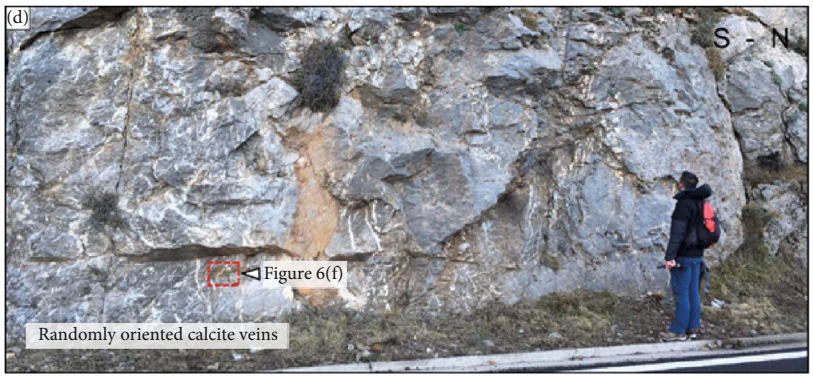

(d)

Figure 5: (a) Sketch of the spatial distribution of veins within the outcrop. In the footwall, three systematically oriented vein systems (F1 to F3) (b) evolve to randomly oriented veins located next to the fault core (c). In the hanging wall, only randomly oriented veins are observed (d).

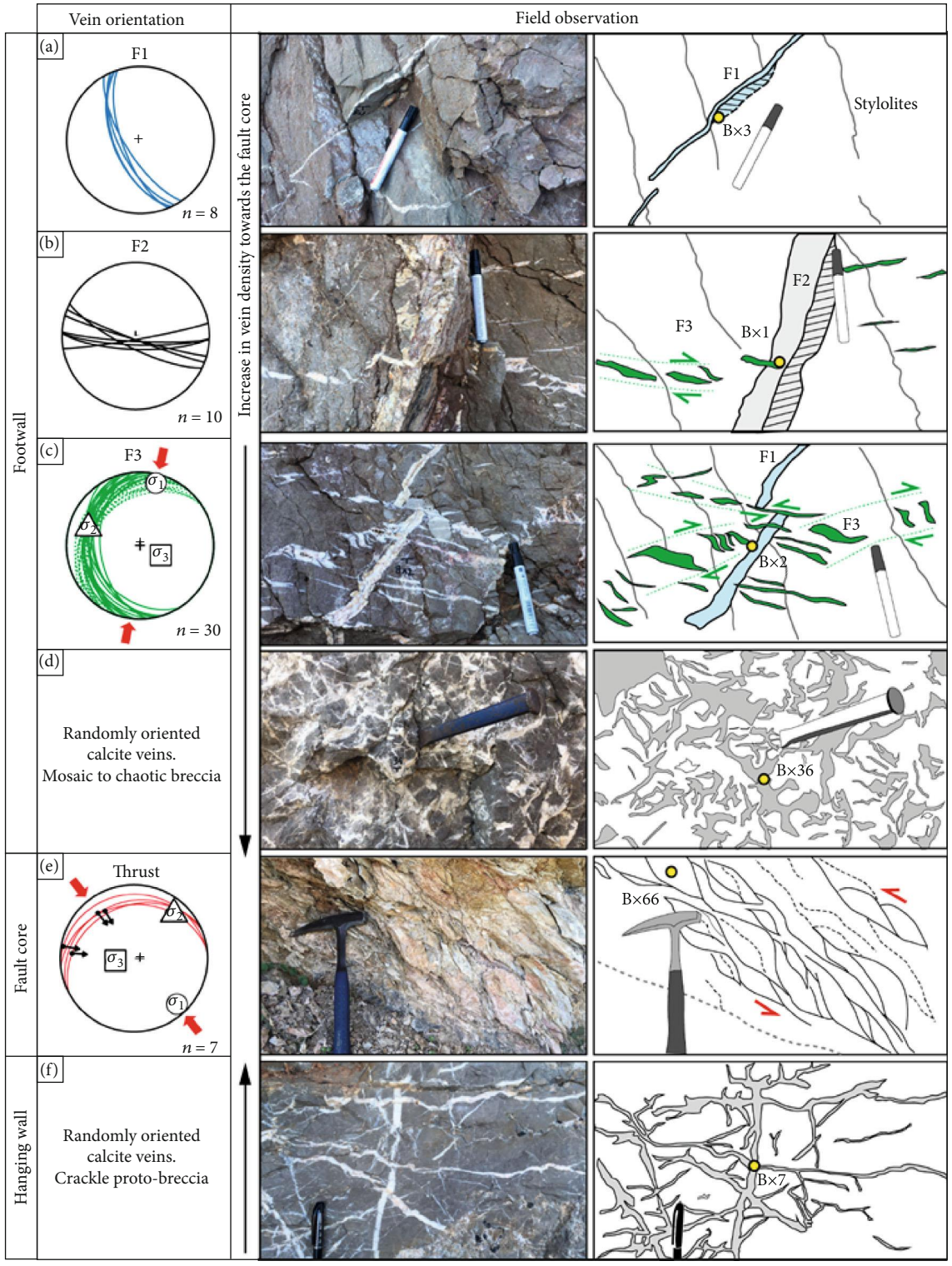

Figure 6: Spatial distribution and crosscutting relationships between veins developed within the studied thrust zone. Vein density increases towards the fault plane. In the footwall, three vein systems (F1, F2, and F3) (a, b, and c, respectively) evolve to randomly oriented veins (d) on approaching the fault core (e). In the hanging wall, only randomly oriented veins are observed, being more chaotic towards the fault plane (f). The yellow circle refers to sample location.

locates immediately below the fault core (Figure 5(a)), strikes E-W, dips between 15 and 30°N, and has a displacement of several hundred meters juxtaposing the Cenomanian-Turonian sequence of the hanging wall against the Coniacian succession of the footwall [38, 42] (Figures 3 and 5). The fault core overlying the slip plane consists of a 2 to 7 m thick, light

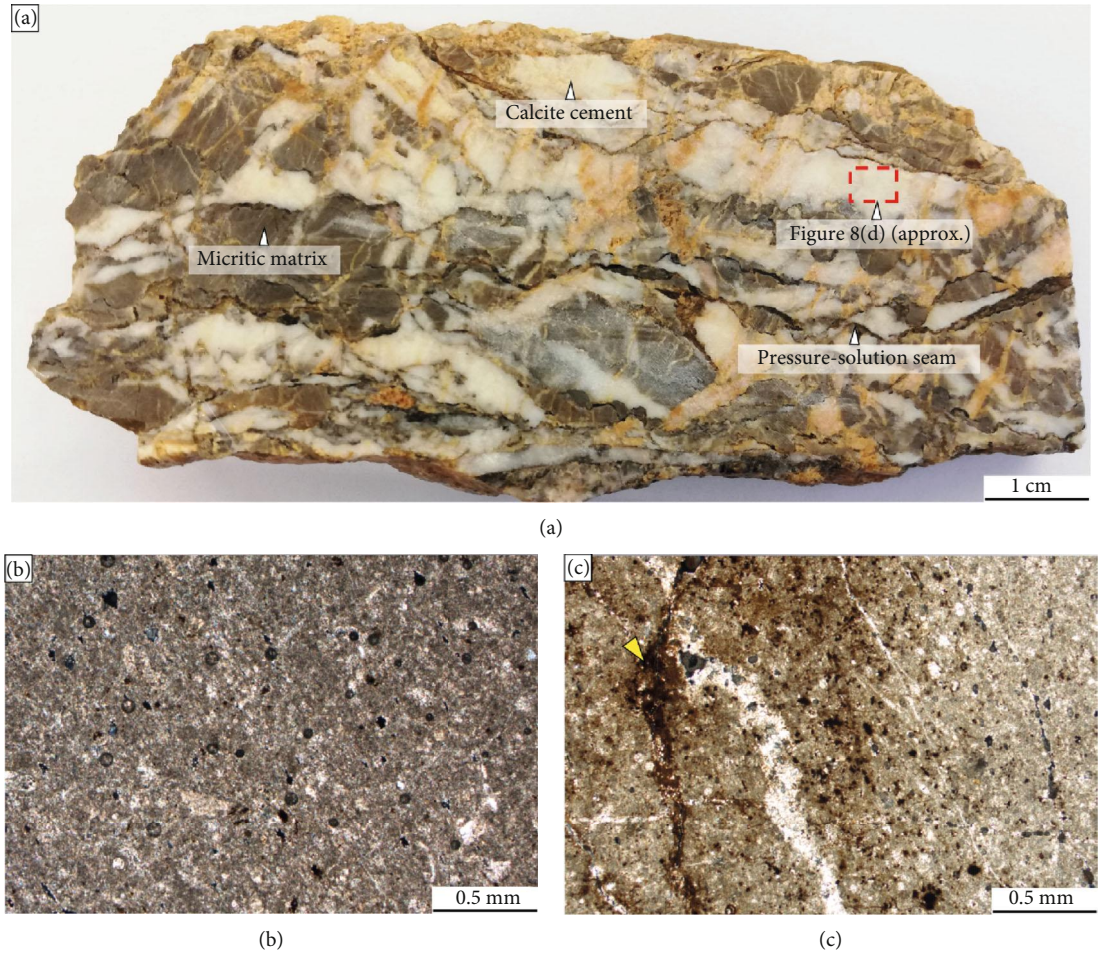

Figure 7: Fault core images. (a) Hand sample photograph of the foliated cataclasite showing S-C shear lenses (lithons) of grey host rock micritic limestone and calcite, bounded by dissolution seams or stylolites. Detail of the calcite cement can be found in Figure 8(d). (b, c) Optical microphotographs of the foliated cataclasite matrix with the presence of reddish clay minerals concentrated along pressure solution surfaces (yellow arrow).

grey to yellowish foliated cataclasite (Figure 7). This foliated cataclasite is characterized by well-developed S-C shears forming sigmoidal lenses (imbricated lithons), a combination of host rock carbonate and calcite lenses within a fine-grained micritic matrix (Figure 7(b)) with abundant calcite cement (Figures 6(e) and 7). Imbricated lithons are bounded by well-developed pressure-dissolution seams or stylolites (Figure 7(a)). S-C shears and stylolites strike ENE-WSW, compatible with the NNW-SSE shortening direction. Orange to reddish clay minerals concentrate along pressure-dissolution surfaces and are locally scattered within the micritic matrix (Figure 7(c)).

The transition from the fault core to the hanging wall damage zone is marked by discrete S-C sigmoidal shears without the development of foliated cataclasite, or by a discrete, discontinuous slip plane mineralized with calcite (Figure 5(c)).

Both the footwall and hanging wall damage zones comprise multiple sets of systematically and randomly oriented calcite-cemented fractures (i.e., veins) developed at both sides of the fault core (Figures 5 and 6). Although in both cases, there is a progressive increase in deformation and vein intensity from the protolith towards the fault core (Figure 5(a)), the geometry of veins differs from one to another damage zone.

In the footwall damage zone, there are two areas showing different vein characteristics (Figure 5(a)). The first area is around 30 m wide from the protolith and is characterized by three systematically oriented vein systems (F1 to F3) with clear crosscutting relationships between them (Figures 5(a)–5(c)). F1 consists of NNW-SSE extensional veins dipping between 50 and 70° to the SW. They are up to 1–2 m long and less than 2 cm thick (Figures 5(a), 5(b), and 6(a)). F2 is characterized by E-W extensional veins steeply dipping to the S-SW. These veins are several meters long and up to 5 cm thick (Figures 5(a), 5(b), and 6(b)). F3 consists of N-S and NE-SW *en échelon* conjugate sets of tension gashes (i.e., hybrid extensional-shear calcite veins) gently dipping towards the NW (Figure 6(c)). These veins are centimetric-sized and have sigmoidal shapes. The second area observed in the footwall covers around 15-20 m between the first area and the fault core and is dominated by randomly oriented calcite veins defining a dilational mosaic to chaotic breccia [52] (Figure 6(d)).

By contrast, in the hanging wall, the damage zone is narrower, only concentrated in the 15-20 meters near the fault core (Figure 6(e)), and it is defined by randomly oriented calcite veins defining an incipient crackle breccia (proto-breccia) [52] (Figure 6(f)). Fracture density is lower than within the footwall damage zone.

4.3. Calcite Cements of Veins and Breccias. The damage zones in the footwall and hanging wall not only differ in the type and distribution of fracture systems, as previously described, but also they also show different fracture-filling calcite cements, characterized by distinct petrological and geochemical features.

In the footwall, three calcite cement generations (Cc1 to Cc3) have been observed filling the fracture systems F1 to F3 and two of those calcite cements (Cc1 and Cc2) are also present in the mosaic to chaotic breccia (randomly oriented fractures).

Calcite cement Cc1 exhibits a milky to slightly brownish color in hand sample and consists of up to 1 mm-sized anhedral crystals showing mechanical twinning and featuring a blocky to elongated blocky texture, in which crystals grow syntaxially. This cement shows a dark to light orange cathodoluminescence (Figure 8(a)). Calcite Cc1 precipitated in fractures F1 and in the mosaic to chaotic breccia of the footwall.

Cc2 displays a white to translucent aspect in hand sample. It is formed of anhedral to subhedral calcite crystals, ranging in size from approximately 0.2 to 5 mm, with a blocky to elongated blocky texture. The elongated blocky Cc2 cement grows syntaxially from the fracture walls (Figures 8(a) and 8(b)). Crystals present abundant twin planes and show a nonluminescent to bright orange concentric zonation under cathodoluminescence in which the zoning pattern generally coincides with the crystal growth (Figure 8(b)). Calcite Cc2 precipitated in fractures F2 as well as in fractures F1 and in the mosaic to chaotic breccia of the footwall after Cc1.

Cc3 exhibits a milky appearance in hand sample and is constituted of up to 0.5 mm anhedral blocky, locally elongated crystals. It has mechanical twinning and presents a dull orange luminescence (Figure 8(c)). Cc3 precipitated in fractures F3.

On the other hand, in the hanging wall and in the fault core, only one calcite cement (Cc4) is observed. Cc4 precipitated in the main fault plane and in randomly oriented fractures. This cement has a milky aspect in hand sample and is characterized by up to 1 mm anhedral crystals with a nonluminescent to dark brown luminescence (Figure 8(d)).

4.4. Oxygen and Carbon Isotopes. The $\delta^{18}O$ and $\delta^{13}C$ isotopic composition of the calcite cements Cc1 to Cc4, adjacent host rocks, and fault rocks is summarized in Table 1 and presented in Figure 9. The calcite cement Cc0 in the interparticle porosity of the grainstone from the Collada Gassó Formation (footwall) has $\delta^{18}O$ values between -7.2 and -6.7‰VPDB and $\delta^{13}C$ values between -0.5 and +0.7‰VPDB. The micrite matrix of the wackestone from the Santa Fe Formation (hanging wall) shows $\delta^{18}O$ values between -6.2 and -5.8‰ VPDB and $\delta^{13}C$ values between +2.1 and +2.2‰VPDB. The carbonate micritic matrix from the cataclasite yields $\delta^{18}O$ values between -7.1 and -6‰VPDB and $\delta^{13}C$ values between +2.3 and +3‰VPDB.

The calcite cements Cc1 to Cc4 exhibit a wider range of values (Figure 9). Cc1 has $\delta^{18}O$ values ranging between -8.2 and -6.5‰VPDB and $\delta^{13}C$ values between -2 and -1.5‰ VPDB. Cc2 is characterized by $\delta^{18}O$ values between -8.2 and -5.4‰VPDB and $\delta^{13}C$ values between -6.3 and -3.3‰ VPDB. Cc3 shows $\delta^{18}O$ values between -13 and -11.7‰ VPDB and $\delta^{13}C$ values between -3.2 and -1.9‰VPDB and Cc4 has $\delta^{18}O$ values between -13.1 and -11.9‰VPDB and $\delta^{13}C$ values between -0.6 and +2.4‰VPDB. Calcite cements precipitated in the footwall (Cc1, Cc2, and Cc3) exhibit negative $\delta^{13}C$ isotopic values, whilst the calcite cement precipitated within the fault plane and hanging wall (Cc4) displays heavier $\delta^{13}C$ values (Figure 9(a)). In addition, the $\delta^{18}O$ values also exhibit two different trends within the four calcite cements: Cc1 and Cc2 show $\delta^{18}O$ values similar to those of Cc0 and host rocks (Figures 9(a) and 9(b)), whereas Cc3 and Cc4 have lighter $\delta^{18}O$ values with respect to the host carbonate values (Figures 9(a) and 9(b)).

4.5. Clumped Isotopes. Temperatures in °C and $\delta^{18}O_{fluid}$ in ‰ VSMOW of the vein-forming fluids are calculated from the measured Δ_{47} using the formula of [54, 55], respectively (Table 1 and Figure 10). The Δ_{47} value for Cc1 ranges between 0.619 and 0.642, which translates into temperatures of 42–51°C and $\delta^{18}O_{fluid}$ of -1.8 to -0.1‰VSMOW. For Cc2, Δ_{47} is between 0.562 and 0.589, implying temperatures between 64 and 78°C and $\delta^{18}O_{fluid}$ between +3.7 and +5.9‰VSMOW. For Cc3, Δ_{47} varies between 0.498 and 0.515, which translates to temperatures between 105 and 117°C and $\delta^{18}O_{fluid}$ between +3.2 and +5.5‰VSMOW. Finally, Δ_{47} values of Cc4, between 0.53 and 0.535, imply temperatures of 93 to 96°C and $\delta^{18}O_{fluid}$ between +0.7 and +1.9‰VSMOW. In the footwall, the calculated temperatures progressively increase from Cc1 to Cc3 and the $\delta^{18}O_{fluid}$ is lighter in Cc1, whilst Cc2 and Cc3 have a similar value.

4.6. Strontium Isotopes. A selected number of samples from each calcite cement generation (Cc0 to Cc4) and related host rocks were analyzed for Sr isotopic composition (Table 1 and Figure 11). Cc0 (in the footwall host rocks) has a $^{87}Sr/^{86}Sr$ ratio of 0.707606, whereas host rocks from the hanging wall have a $^{87}Sr/^{86}Sr$ ratio of 0.707718. These values fall within the range of values expected for Upper Cretaceous marine carbonates [56] (Figure 11(b)).

The calcite cements in the footwall exhibit higher $^{87}Sr/^{86}Sr$ ratios with respect to the calcite cement (Cc0) cementing their adjacent host rock (Figure 11(a)). This ratio is 0.707707 for Cc1, ranges from 0.707695 to 0.707699 for Cc2, and is 0.707698 for Cc3. By contrast, the calcite cement Cc4 has a $^{87}Sr/^{86}Sr$ ratio similar to its adjacent host carbonate in the case of the crackle proto-breccia veins located in the hanging wall (0.707715) and more radiogenic than the host rock in the case of the fault plane (0.707771) (Figure 11(a)).

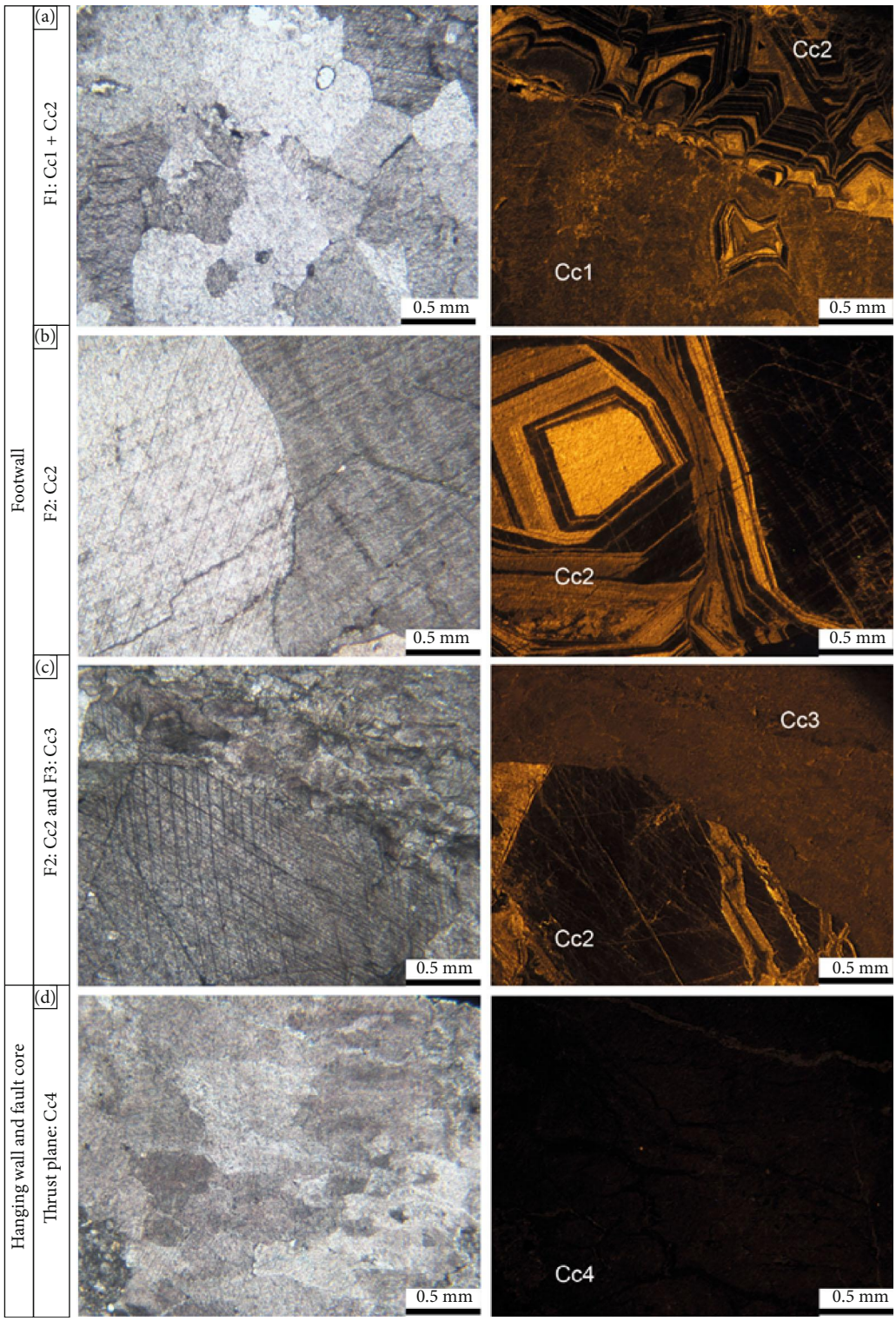

Figure 8: Paired optical and CL microphotographs from calcite cements precipitated within the fault core and fault damage zone of the studied thrust. (a) Fracture F1 cemented by calcite cements Cc1 and Cc2. (b) Calcite cement Cc2, with its characteristic CL zonation, filling a fracture F2. (c) Cc3 filling a F3 fracture, postdating a fracture F2 filled with Cc2. (d) Cc4 in the main fault plane.

4.7. Elemental Composition. The elemental composition (Ca, Mg, Fe, Mn, and Sr), including rare earth elements (REE) and yttrium (Y), was measured for each calcite cement generation and their host carbonates and the results are presented in Tables 2 and 3 and in Figure 12. In general, the trace element compositions widely vary depending on the calcite cement,

Table 1: $\delta^{18}O$, $\delta^{13}C$, and $^{87}Sr/^{86}Sr$ isotopic signature of the calcite cements, fault rocks, and host rocks. The Δ_{47}, $\delta_{18}O_{fluid}$, and precipitation temperatures obtained from clumped isotopes are also included. Fw means footwall and Hw means hanging wall.

Sample	Fracture	Cement	$\delta^{18}O$ ‰VPDB	$\delta^{13}C$ ‰VPDB	$^{87}Sr/^{86}Sr$	Δ_{47}	$\delta_{18}O_{fluid}$ ‰VSMOW	T (°C)
Bx1B	F2	Cc1	-8.2	-1.7	0.707707	0.619/0.642	-1.8 to -0.1	42 to 51
Bx 3	F1	Cc1	-7.3	-1.8				
Bx36.I	Breccia (Fw)	Cc1	-7.6	-2				
Bx36.IV	Breccia (Fw)	Cc1	-7.4	-1.6				
Bx36.V	Breccia (Fw)	Cc1	-6.5	-1.5				
Bx3.III	F1	Cc2	-8.2	-3.7				
Bx1A.I	F2	Cc2	-7	-4.6	0.707699	0.562/0.589	+3.7 to +5.9	64 to 78
Bx1B.II	F2	Cc2	-6.3	-4.6				
Bx3.II	F1	Cc2	-7	-3.3				
Bx36.II	Breccia (Fw)	Cc2	-7.8	-5.6	0.707695			
Bx36.III	Breccia (Fw)	Cc2	-7.2	-6.3				
Bx35	F2	Cc2	-5.4	-4	0.707765			
Bx1A.II	F3	Cc3	-13	-1.9				
Bx2A	F3	Cc3	-12.1	-2.9	0.707698	0.498/0.515	+3.2 to +5.5	105 to 117
Bx2B	F3	Cc3	-11.9	-2.8				
Bx4	F3	Cc3	-11.7	-3.2				
Bx5	Thrust plane	Cc4	-12.9	+0.4	0.707771	0.53/0.535	+0.7 to +1.9	93 to 96
Bx6	Breccia (Hw)	Cc4	-12.3	+2.4				
Bx7.I	Breccia (Hw)	Cc4	-13.1	+0.4	0.707715			
Bx7.II	Breccia (Hw)	Cc4	-11.9	+0.9				
Bx 8	Breccia (Hw)	Cc4	-12.3	-0.6				
Bx66.C	Slip plane	Cc4	-12	+1.6				
Bx1.HR	Host rock (Fw)	Cc0	-7.2	-0.5				
Bx2A.HR	Host rock (Fw)	Cc0	-6.7	+0.7	0.707606			
Bx3.HR	Host rock (Fw)	Cc0	-7	+0.1				
Bx7	Host rock (Hw)		-5.8	+2.2				
Bx8	Host rock (Hw)		-6.2	+2.1	0.707718			
Bx6.I	Fault rock (matrix)		-6.9	+2.9				
Bx6.II	Fault rock (matrix)		-7.1	+3				
Bx66	Fault rock (matrix)		-6.6	+2.6				
Bx67	Fault rock (matrix)		-6	+2.3				

whilst the REY (REE and Y) pattern in the four cements follows a trend comparable to that of the adjacent host rock (Figure 12(c)).

In the footwall, the calcite cements Cc1 and Cc2 are characterized by low Mg and Sr contents, intermediate Mn, and variable Fe concentrations, whereas Cc3 has high Mn and Fe contents, intermediate Mg values, and variable-high Sr concentrations (Figure 12(a)). The REY concentration of these cements (Cc1 to Cc3) is lower compared to that of the cement within the host rock (Cc0), but follows a similar flat trend, with a slight negative Ce anomaly (Figures 12(b) and 12(c)) and a slight positive Y anomaly (except for Cc2 that may exhibit either a positive or negative Ce anomaly) (Figure 12(c)).

In the fault core and hanging wall, Cc4 exhibits high Mg and Sr concentrations, intermediate Fe values, and low Mn contents. The REY pattern of Cc4 is also flat with a better defined negative Ce anomaly and a positive Y anomaly, which are also present in the hanging wall host rock. The REY concentrations are lower in cement Cc4 than in its adjacent host rocks, except for the calcite in the fault plane that exhibits higher concentrations (Figure 12(c)).

Mg/Ca and Sr/Ca molar ratios of the parent fluids that precipitated the calcite cements were calculated using the formula of [57] for low temperature (25–40°C) and for higher temperature (90–100°C) of precipitation using distribution coefficients ($K_{Mg} = 0.012$ at 25°C [58], $K_{Mg} = 0.1163$ at 90°C [59], $K_{Sr} = 0.054$ at 25°C [60], and $K_{Sr} = 0.08$ at 100°C [61]). The obtained molar ratios are presented in Table 2.

4.8. Neodymium Isotopes. Nine representative samples from calcite cements and related host rocks were also analyzed for Nd isotopic composition. However, although the Nd concentration is above the detection limit for all the analyzed samples (Table 3), the $^{143}Nd/^{144}Nd$ ratio could not be measured. This is attributed to both the low Nd concentration

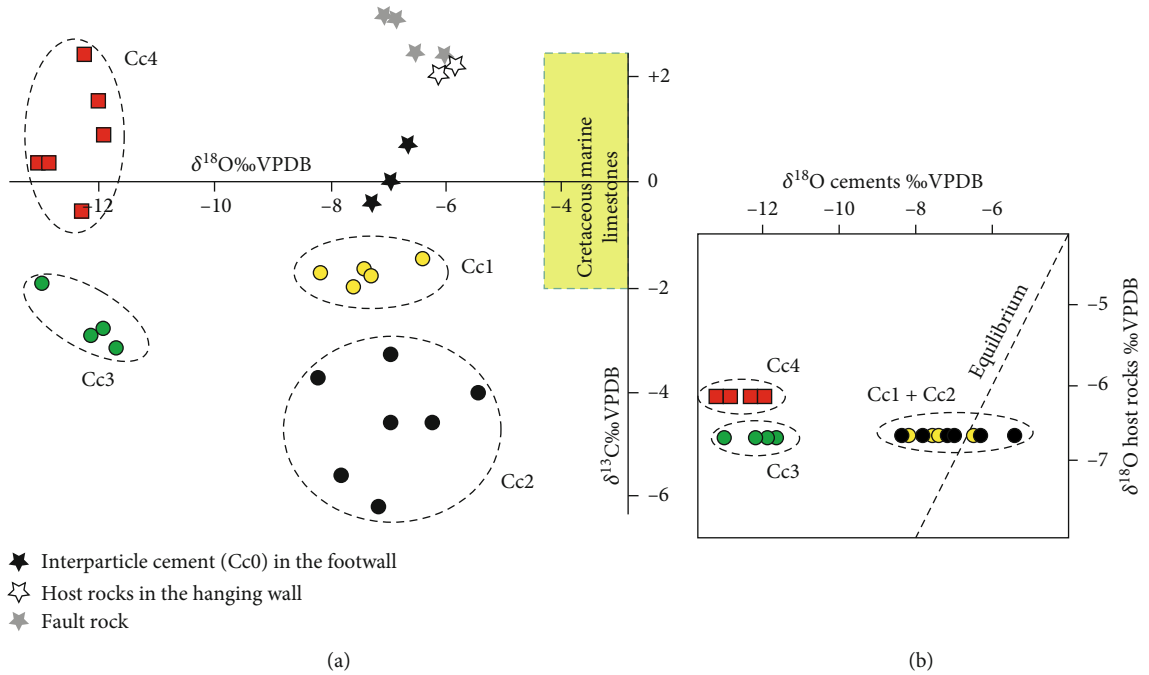

Figure 9: (a) Crossplot showing the $\delta^{18}O$ and $\delta^{13}C$ compositions of the calcite cements, host rocks, and fault rocks (carbonate matrix from the cataclasite). Cretaceous marine limestone values (green box) are from [53]. (b) $\delta^{18}O$ values of the calcite cements versus $\delta^{18}O$ values of the related host rocks.

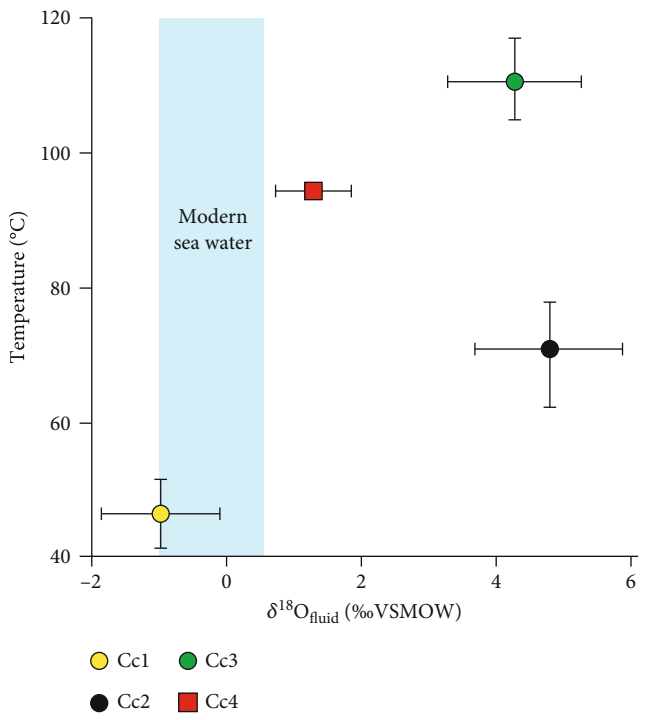

Figure 10: Temperatures (°C) vs. $\delta^{18}O_{fluid}$ (‰VSMOW) calculated from clumped isotope thermometry for calcite cements Cc1 to Cc4.

in the samples, ranging between 0.5 and around 10 ppm (Table 3), and the scarce quantity of sample that was possible to collect, generally around 30 mg, which was not enough for a dynamic multicollection method through 160 cycles at a stable intensity of 1 V.

5. Discussion

5.1. Dissolution versus Precipitation Zones. The studied fault zone has different brittle structures accommodating deformation both in the fault core and in the damage zone. Within the fault core, the presence of tectonic stylolites and S-C structures evidences processes of pressure solution and/or frictional sliding [54, 55]. Such processes are associated with contractional stress concentration and slip accommodation imposed by the advancing thrust [64, 65]. By contrast, within the damage zone, the widespread presence of veins represents dilational sites where calcite precipitated [66, 67]. The mechanism of calcite precipitation was likely induced by the rapid fluid pressure drop due to fluid trapping in the fractures developed in the footwall and hanging wall [10, 66, 68, 69]. The repartition of such structures, stylolites, S-C foliation, and veins, and therefore of zones of dissolution and zones of precipitation, is the result of a heterogeneous distribution of stress and the variation in deformation intensity across the fault zone [54].

5.2. Structural Context of Fracturing and Veining. The main stress orientations responsible for the development of the studied thrust system have been calculated plotting the main plane orientation and related slickenlines (Figure 6(e)). The estimated stress field shows a SSE transport direction, compatible with the N-S to NNW-SSE shortening direction reported in the Pyrenees [28, 30, 39], and a vertical minimum principal stress ($\sigma_v = \sigma_3$), characteristic of compressional regimes [9, 10]. The studied vein systems are interpreted as developed during the thrust activity under the same compressional regime [8, 42, 70]. The synchronicity between

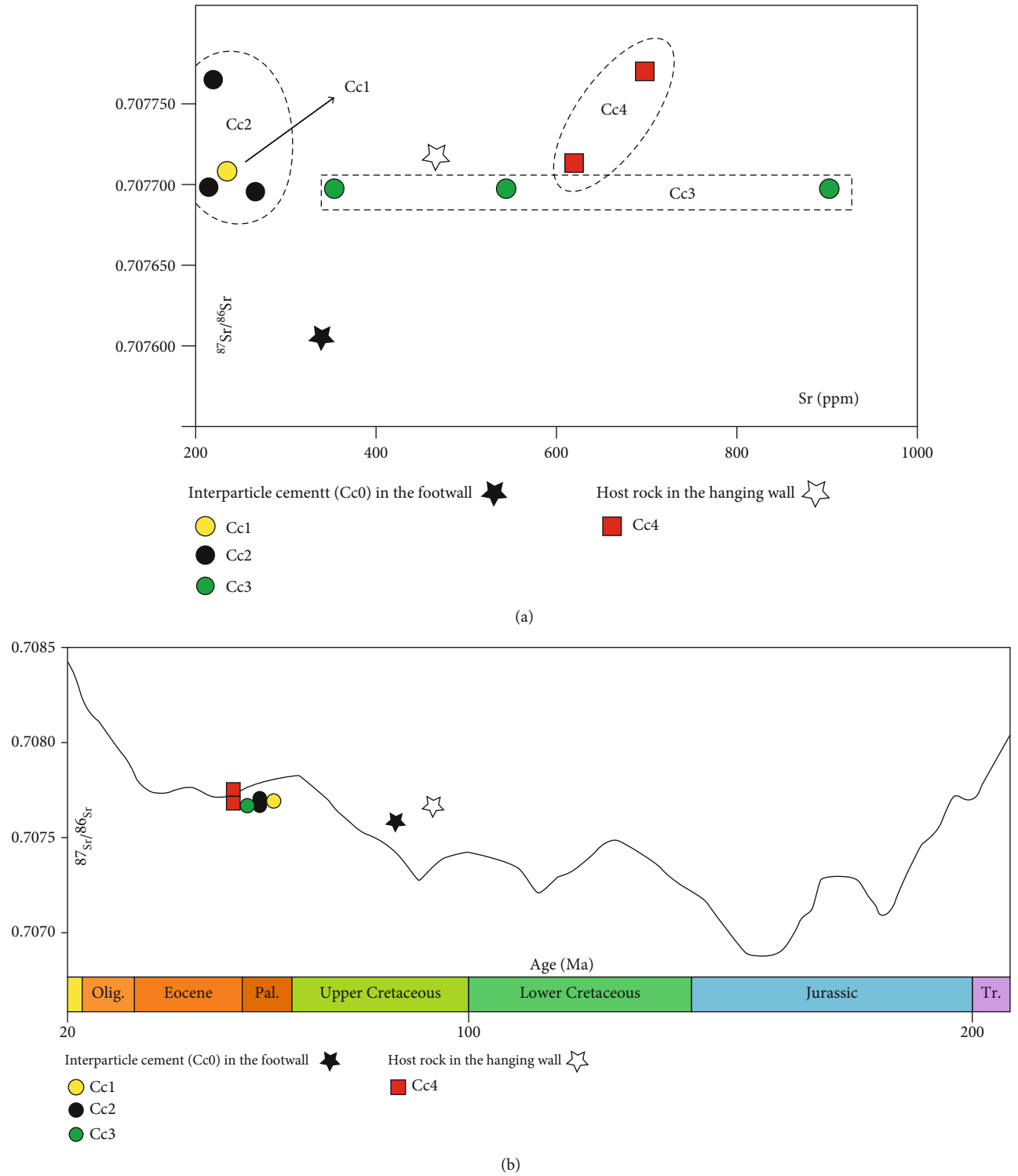

FIGURE 11: (a) $^{87}Sr/^{86}Sr$ isotopic ratios of calcite cements and host carbonates plotted against the Sr content. (b) $^{87}Sr/^{86}Sr$ ratios compared with the $^{87}Sr/^{86}Sr$ isotopic ratios of seawater through time from the LOWESS curve [56].

thrusting and veining is supported by the exclusive presence of veins in the damage zone as well as by the gradual increase in vein density and slight change in strike when approaching the main thrust plane. However, the steeply dipping orientation of F1 and F2 with respect to the subhorizontal σ_1 axis differs with theoretical models that describe the formation of flat-lying extensional fractures that open in the σ_3 vertical direction (i.e., oriented parallel to the σ_1 axis) [9, 10, 13, 68, 71]. Despite this apparent discrepancy, the presence of the same calcite cements (Cc1 and Cc2) in F1-F2 fractures and in the mosaic to chaotic breccia developed along the fault plane corroborates the synchronicity between thrusting and

Table 2: Elemental composition (Ca, Mg, Fe, Mn, and Sr) of the different calcite cements (Cc1 to Cc4), the interparticle cement Cc0 in the footwall host rocks (FW), and the hanging wall rocks (HW). The calculated Mg/Ca and Sr/Ca molar ratios of the parent fluid using the distribution coefficient equation [57] are also shown.

Sample	Ca (ppm)	Mg (ppm)	Fe (ppm)	Mn (ppm)	Sr (ppm)	Mg/Ca low T	Mg/Ca high T	Sr/Ca low T	Sr/Ca high T
Cc1	37236	859.7	2518.8	236.8	239	0.317	0.033	0.0049	0.0037
Cc2	378096	921.1	1249.4	222.3	216.2	0.335	0.035	0.0044	0.0033
Cc2	385024	741.0	1188.8	151.5	219.5	0.264	0.027	0.0043	0.0033
Cc2	393269	865.9	564.1	86.6	270.7	0.303	0.031	0.0052	0.0039
Cc3	387653	1912.4	2967.2	380.5	906.8	0.678	0.070	0.0178	0.0134
Cc3	300362	1997.7	2704.6	409.3	548.1	0.914	0.094	0.0139	0.0104
Cc3	350768	1397.6	2997.7	661.1	356.1	0.548	0.056	0.0077	0.0058
Cc4	322604	3637.8	2345.2	97.3	699.5	1.550	0.160	0.0165	0.0124
Cc4	366243	1908.1	1658.3	80.3	623.6	0.716	0.074	0.0130	0.0097
Cc4	346495	1784.2	1298.2	65.2	625.3	0.708	0.073	0.0138	0.0103
FW	298763	3376.3	3248.8	345.6	340.8	1.553	0.160	0.0087	0.0065
HW	321638	2968.0	980.1	68.8	468.9	1.268	0.131	0.0111	0.0083

Table 3: REE and Y contents of the different calcite cements (Cc1 to Cc4), the interparticle cement Cc0 from the footwall (FW), and the host rocks from the hanging wall (HW). Values are given in ppm. *DL: detection limit.

Sample	La	Ce	Pr	Nd	Sm	Eu	Gd	Tb	Dy	Y	Ho	Er	Tm	Yb	Lu
DL*	0.21	0.32	0.04	0.15	0.03	0.01	0.02	0.003	0.02	0.2	0.003	0.01	0.002	0.01	0.01
Cc1	7.13	13.46	1.81	6.01	1.38	0.26	1.35	0.19	1.05	7.04	0.17	0.45	0.08	0.37	0.06
Cc2	3.03	9.96	0.85	3.00	0.75	0.14	0.66	0.08	0.43	3.31	0.07	0.19	0.03	0.16	0.03
Cc2	3.48	4.35	1.07	3.81	0.95	0.20	0.88	0.13	0.71	5.43	0.12	0.35	0.06	0.30	0.05
Cc2	0.81	1.26	0.17	0.59	0.23	0.04	0.17	0.02	0.15	1.29	0.03	0.07	0.01	0.06	<LD
Cc3	6.15	10.73	1.64	5.77	1.36	0.26	1.21	0.17	0.92	6.53	0.15	0.39	0.06	0.31	0.05
Cc3	5.22	9.19	1.22	4.38	0.95	0.19	0.96	0.13	0.72	5.44	0.12	0.32	0.05	0.24	0.04
Cc3	1.31	2.38	0.38	1.45	0.37	0.08	0.33	0.04	0.25	2.37	0.05	0.13	0.02	0.10	0.02
Cc4	2.73	6.03	0.86	2.89	0.69	0.13	0.58	0.08	0.43	3.35	0.07	0.19	0.03	0.15	0.02
Cc4	0.78	1.05	0.17	0.58	0.24	0.04	0.14	0.02	0.14	1.87	0.03	0.09	0.02	0.08	<LD
Cc4	2.08	1.84	0.53	1.82	0.44	0.08	0.36	0.05	0.25	2.45	0.05	0.14	0.03	0.13	0.02
Cc0	9.83	23.27	3.04	10.56	2.44	0.49	2.16	0.28	1.52	8.70	0.22	0.61	0.11	0.51	0.08
HW	2.39	3.52	0.52	1.75	0.41	0.07	0.36	0.05	0.33	3.23	0.06	0.18	0.03	0.17	0.03

fracturing. In the case of conjugated fracture systems F3, their bisector angle indicates a subhorizontal σ_1 and a subvertical σ_3, and therefore, their formation is compatible with the prevailing stress field associated with thrusting ($\sigma_v = \sigma_3$).

Two mechanisms, a local variation of the stress axes as well as high fluid pressure conditions, are invoked to explain the formation of the steeply dipping F1 and F2 fractures in relation to the low angle reverse fault [72–74]. In the first case, the remote stress fields could have varied locally within a constant far-field compressional regime to become properly oriented for the development of these fractures [71, 72, 75]. Such a local variation of the magnitude and orientation of the remote stress fields is attributed to the formation of a process zone at the front of the fault tip during thrust (slip plane) propagation [71, 76]. This occurs, firstly, because the fault tip acts as a stress concentrator amplifying the magnitude of the remote stress [76] and, secondly, because the main compressive stress (σ_1) exhibits different angles with the fault in compressive quadrants with respect to dilational quadrants in propagating faults [71, 76].

Several observations, which are described below, indicate that the formation of the studied fractures occurred under high fluid pressure conditions, and therefore, it is associated with a hydraulic (over)pressure mechanism. Fluid overpressure may explain the high concentration of systematically oriented extensional (F1, F2) and extensional-shear (F3) veins, as well as the absence of any structural orientation of veins in the breccias [77]. Comparable fracture systems (systematic arrays of extensional and extensional-shear fractures) are expected to develop in compressional settings when the tensile overpressure condition is achieved, that is, when the pore fluid pressure exceeds the least compressive stress ($P_f > \sigma_3$) [9, 10, 78]. Such a fluid pressure is common during the propagation of thrust faults in compressional regimes [9, 12, 67, 79] and is attributed to the following: (i) the constraint stress field around the fault tip may generate overpressure of a confined fluid [80, 81], (ii) the low dip of

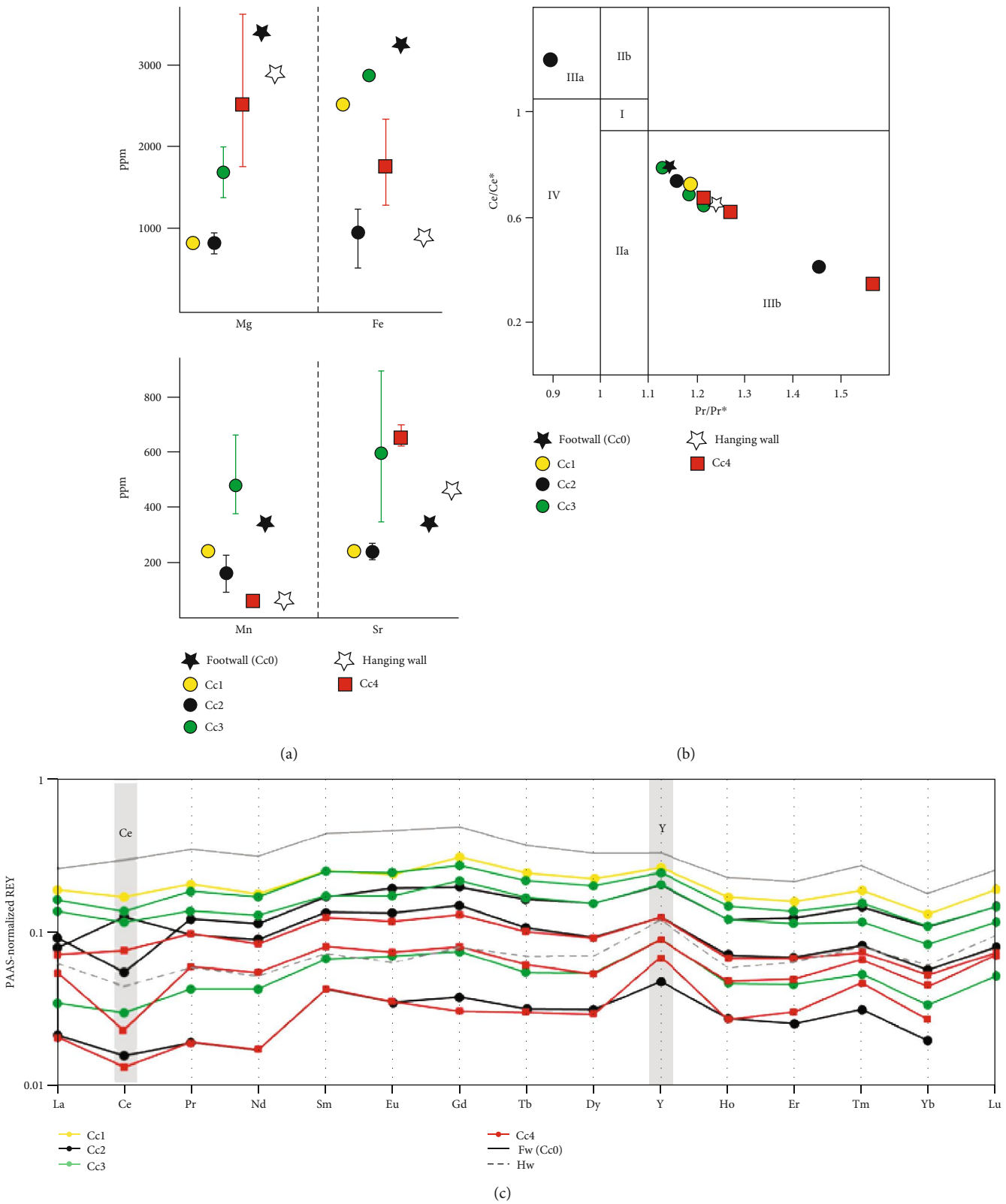

Figure 12: (a) Elemental composition (Mg, Fe, Mn, and Sr) in ppm of calcite cements and host rocks. Bars indicate maximum, minimum, and average composition. (b) PAAS-normalized Ce/Ce* vs. Pr/Pr* crossplot showing the Ce and Pr anomalies of calcite cements and host rocks using the method of [62] modified by [63]. Field I: no anomaly. Field IIa: positive La anomaly and no Ce anomaly. Field IIb: negative La anomaly and no Ce anomaly. Field IIIa: positive Ce anomaly. Field IIIb: negative Ce anomaly. Field IV: positive Ce and La anomalies. (c) PAAS-normalized rare elements and yttrium (REY) patterns of calcite cements and host rocks.

thrusts prevents vertical flow [14, 68], and (iii) it is because of sediment compaction induced by loading during thrust sheet emplacement [77, 81].

5.3. Fluid History and Pathways. The widespread presence of calcite cements in the different fracture sets indicates that these structures themselves were traps for fluids migrating during thrusting. Field observations based mainly on the macroscopic vein features and crosscutting relationships between them together with the above presented petrological and geochemical data evidence the formation of four calcite cementation phases (Cc1 to Cc4) that record the evolution of the fluid system during the thrust activity. Since the footwall and hanging wall exhibit different fracture systems and different calcite cements, the fluid system was compartmentalized [26, 27, 82, 83].

5.3.1. Fluid System in the Footwall. The evolution of the fluid system in the footwall during thrusting is inferred from the geochemical data of calcite cements Cc1, Cc2, and Cc3.

Calcite cement Cc1 is observed within fractures F1 and within the mosaic to chaotic breccia located in the footwall. This cement has $\delta^{18}O$ (-8.2 to -6.5‰VPDB) and $\delta^{13}C$ values (-2 to -1.5‰VPDB) similar or slightly more depleted with respect to those of the interparticle calcite cement (Cc0) in the adjacent host rocks (Figures 9(a) and 9(b)). This fact, together with the observed positive Y anomaly in both Cc1 and Cc0, indicates buffering of the vein-forming fluids by the adjacent host carbonates due to fluid-rock interaction [84]. The fluid-rock interaction is also recorded in the $\delta^{18}O_{fluid}$ obtained from clumped isotopes, yielding values between -1.8 and -0.1‰VSMOW. These values may result from interaction between meteoric waters, which have typically negative $\delta^{18}O$ values, and marine carbonates, with $\delta^{18}O$ values around 0‰PDB [64]. This fact is supported by the calculated Mg/Ca and Sr/Ca molar ratios, indicating the involvement of meteoric fluids, and the diluted elemental composition in Cc1 with respect to Cc0, showing lower REY concentration and lower Mg, Mn, and Sr contents (Figure 12(a)). Likewise, the $^{87}Sr/^{86}Sr$ ratio of Cc1 is slightly more radiogenic than Cc0 but is still between the ranges of Cretaceous marine carbonates (Figure 11). The homogeneous orange luminescence of Cc1 is interpreted as constant precipitation rates during a single precipitation event, and the presence of a negative Ce anomaly suggests precipitation in an oxic environment [84] (Figures 12(b) and 12(c)). Finally, the temperature of Cc1, also obtained from clumped isotope thermometry, ranges between 42 and 51°C. The presence of meteoric fluids and the relatively low temperatures could indicate shallow burial depths, probably less than 1 km if we consider a normal geothermal gradient of 25–30°C/km and a surface temperature of 20°C. Therefore, Cc1 precipitated from meteoric fluids (Figure 13(a)) with a composition strongly buffered by the Cretaceous host carbonates.

Calcite cement Cc2 is found in fractures F1 and F2 and within the mosaic to chaotic breccia from the footwall. This cement has similar $^{87}Sr/^{86}Sr$ ratios and $\delta^{18}O$ values to Cc1 but precipitated at higher temperatures (between 64 and 78°C) and from heavier $\delta^{18}O_{fluid}$ (between +3.7 and +5.9‰ VSMOW). These higher temperatures and the $\delta^{18}O_{fluid}$ imply hot formation waters. However, the low $\delta^{13}C$ values (Figure 9), the diluted Mg, Sr, and REY concentrations (Figure 12), and the calculated Mg/Ca and Sr/Ca molar ratios of Cc2 reveal the involvement of meteoric fluids with increasing influence of organic-derived carbon [85–89] (Figure 12(b)). The CL zonation of Cc2, alternating between non- and bright luminescent zones, the presence of positive and negative Ce anomalies (Figures 12(b) and 12(c)), and the oscillations in the Fe and Mn contents (Figure 12(a)) indicate oxidizing-reducing fluctuation, typical of the meteoric environment [6, 90–93]. These facts indicate that Cc2 precipitated from formation fluids that likely evolved from heated meteoric waters during the development of the second fracturing event (F2). The evolution of these fluids probably involved water-rock interactions during progressive increase in burial depths and temperatures linked to thrust sheet emplacement [94–96].

Calcite cement Cc3, occluding fractures F3, shows an $^{87}Sr/^{86}Sr$ ratio similar to cements Cc1 and Cc2 (Figure 11), $\delta^{13}C$ within the same range of values of Cc2 (Figure 9(a)), and a lighter $\delta^{18}O$ than the previous cement generations and the adjacent host carbonates (Figures 9(a) and 9(b)). Such depletion is related to hotter precipitation conditions (between 105 and 117°C). On the other hand, the $\delta^{18}O_{fluid}$ (between +3.2 and +5.2‰VSMOW), the high Sr, Mn, and Fe contents (Figure 12(a)), and the calculated Mg/Ca and Sr/Ca molar ratios for the vein-forming fluids are within the range of formation waters [57, 87, 95]. The homogeneous bright-orange luminescence points to complete precipitation of Cc3 during a single precipitation event [97], and the presence of a negative Ce anomaly indicates oxic precipitation conditions [84] (Figure 12(b)).

In conclusion, the progressive depletion in $\delta^{18}O$ values from Cc1 to Cc3, as well as the continuous increase in precipitation temperatures and enrichment in $\delta^{18}O_{fluid}$ and in the elemental composition, evidences a progressive change in the fluid regime during ongoing deformation. This change may result from a continuous shift in the fluid composition, due to the evolution of the meteoric waters, or from a progressive change in the fluid origin, from percolation of diluted meteoric waters to the upflow of hotter formation fluids. The evolution of the fluid system is also attested by the disequilibrium between Cc3 and its adjacent host rocks (Figure 9(b)) and may be indicative of a continuous opening of the fluid system, which is in turn attributed to the increase in fracture density and superposition of different fracturing events [4, 98–102]. Previous contributions reported the relationships between folding, fracturing, and fluid migration in the eastern part of the Sant Corneli-Bóixols anticline (around the Coll de Nargó area, Figure 1(b)) [37]. During the latest stages of deformation in the frontal part of the anticline, these authors also reported a change in the fluid origin and composition, that is, from percolation of meteoric waters, circulating at approximately 40°C, to migration of hotter formation fluids, at temperatures around 90°C [103]. Consequently, the comparison between both studies suggests a common fluid behavior during the latest-folding to postfolding stages of deformation in the whole anticline.

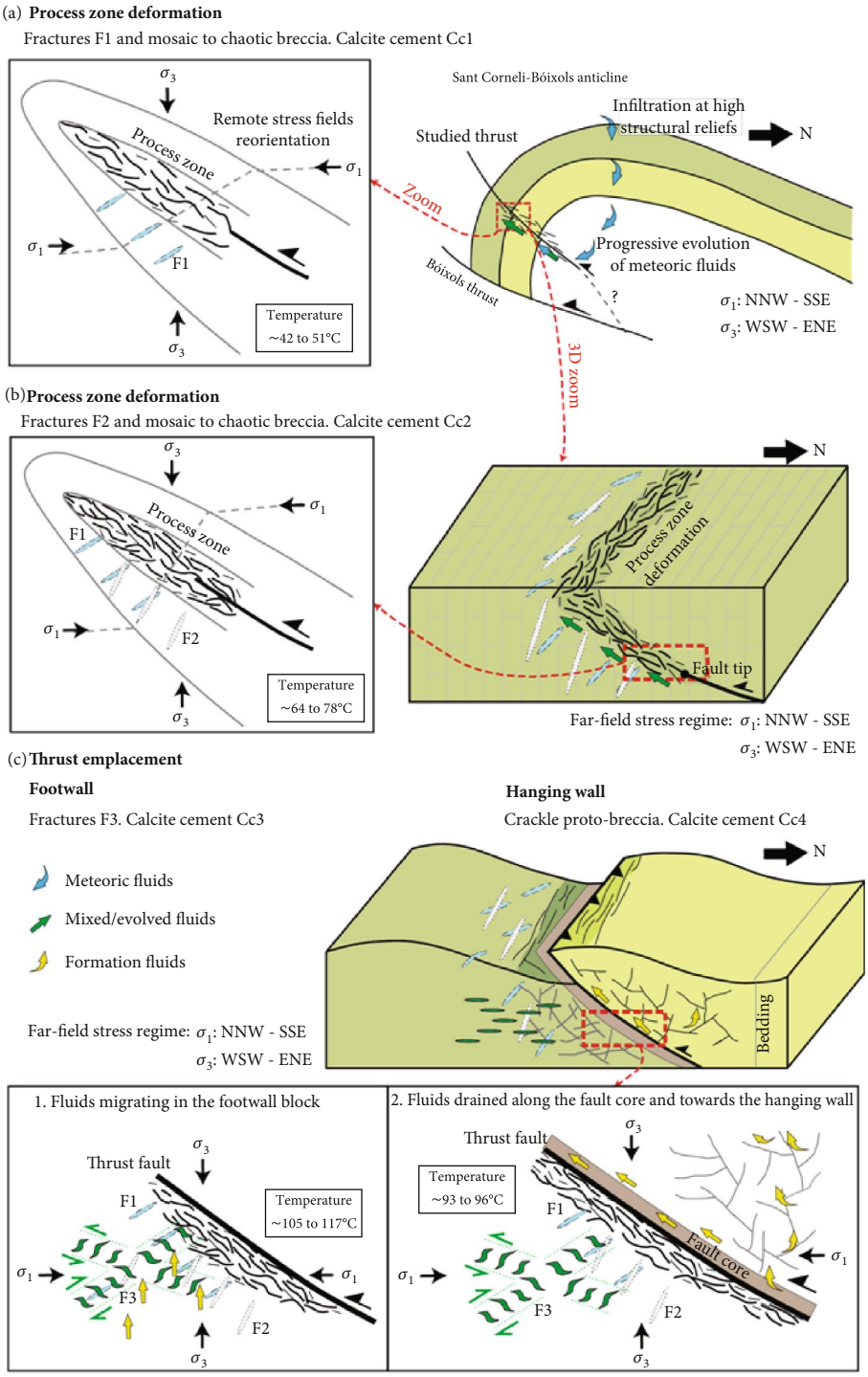

Figure 13: Fluid flow model during the evolution of the studied thrust (not to scale) showing the relationships between synkinematic fracture development, the stress state at each deformation phase, and the involved fluid flow event. (a) During initial fault growth, deformation was concentrated in the process zone (around the fault tip) allowing the formation of fractures F1 and randomly oriented fractures (mosaic to chaotic breccia). During this episode, meteoric fluids infiltrated at high structural reliefs, warmed at depth, and then migrated through diffused deformation around the fault tip. (b) During progressive deformation, new fractures develop and meteoric fluids evolved at increasing depths and temperatures. During these two initial fracturing events (F1-F2), the remote stress field varied locally within the process zone to generate steeply dipping fractures. (c) As the thrust developed, fractures F3 were formed in the footwall damage zone. The orientation of these fractures reflects the far-field stress regime unaltered by faulting. The fluid involved in this stage evidences the continuous increase in precipitation temperatures due to burial during thrust emplacement. From this stage, the thrust drained fluids that only infiltrated in the hanging wall. These fluids were likely expelled from underlying Cretaceous carbonates due to rock compaction during thrusting.

5.3.2. Fluid System in the Hanging Wall. Calcite cement Cc4 precipitated within the main fault plane, within the fault core, and within the randomly oriented fractures (crackle proto-breccia) located in the hanging wall. The similarity between $\delta^{13}C$ values in Cc4 and its host carbonates, together with the high Mg contents and the REY pattern showing a well-defined negative Ce anomaly and a positive Y anomaly, similar to that of the host rocks, indicates buffering of the precipitating fluid by the hanging wall carbonates (Figures 9 and 12). This buffered composition of the fluids is also recorded in the $\delta^{18}O_{fluid}$ obtained from clumped isotopes and yielding values between +0.7 and +1.9‰VSMOW. However, the depletion in $\delta^{18}O$ values in Cc4 in relation to the adjacent rocks suggests that the system was opened to advection of the vein-forming fluid (Figures 9(a) and 9(b)). The Mg/Ca and Sr/Ca molar ratios calculated for the fluid that precipitated Cc4 reveal the presence of formation waters, which precipitated at temperatures between 93 and 96°C (according to clumped isotope thermometry). The $^{87}Sr/^{86}Sr$ ratio of Cc4, similar to that of the hanging wall host rock (0.707718) in the crackle proto-breccia (0.707715), but more radiogenic in the fault plane (0.707771) (Figure 11), reveals a channelized ascending fluid migrating through the thrust plane towards the hanging wall, where it progressively increased the fluid-rock interaction. Cretaceous evaporated seawater is the most probable source for these formation fluids, if we take into account that (i) Cretaceous carbonates are broadly present around and underlying the studied thrust, (ii) the $^{87}Sr/^{86}Sr$ ratios of Cc4 are consistent with Cretaceous seawater and the $\delta^{18}O_{fluid}$ is slightly more enriched with respect to marine values (Figure 10), and (iii) during the Late Cretaceous, there was a transition from marine to lagoonal and thus more restricted and evaporative conditions [104]. Upward migration of Cretaceous connate seawater was also reported during the postfolding stages of evolution in the eastern part of the Sant Corneli-Bóixols anticline [37].

5.4. Thrust Zone Evolution. The successive deformation stages, associated with different fracture systems, record an episodic evolution of the studied thrust zone. We interpret this evolution to result from an upward propagation of the fault tip leading to distributed deformation within the process zone before propagation of the fault [71, 89, 105, 106].

During initial fault growth, deformation at the fault tip, i.e., within the process zone, was dominated by concentration of dilatant (extensional) fracturing, giving rise to fractures F1 and the mosaic to chaotic breccia from the footwall (Figure 13(a)). The fluid associated with this initial deformation stage responsible for precipitation of calcite cement Cc1 was a host-rock buffered meteoric fluid. Meteoric fluids probably infiltrated the system on high structural reliefs that were likely elevated during growth of the Sant Corneli-Bóixols anticline (Figure 13(a)). These fluids warmed up to ~50°C at depth by a normal geothermal gradient and then migrated through diffuse deformation developed in the process zone before the growth and propagation of the thrust slip plane (Figure 13(a)) [71, 89, 105]. As deformation continued, new dilatant fractures F2 developed, and F1 fractures reopened and randomly oriented fractures from the breccia continued forming. This synchronicity is evidenced by the presence of the same calcite cement (Cc2) in the aforementioned fractures. The second fluid flow event, associated with the second deformation stage, was characterized by the progressive evolution of meteoric fluids due to water-rock interactions at increasing depths and temperatures (Figure 13(b)). During these two initial stages of deformation, the remote stress fields varied locally in the process zone, allowing for the formation of steeply dipping fractures (F1 and F2) (Figures 13(a) and 13(b)).

Finally, the thrust slip plane propagated through the process zone. Frictional processes occurred along the thrust surface as well as the progressive weakening of the fault zone, which led to the formation of the foliated cataclasite, characterized by S-C shear fabric, pressure solution seams, calcite mineralization, and carbonate fine-grained matrix. This micritic matrix is petrographically similar to that of the hanging wall protolith (Figures 4(c) and 7(b) and 7(c)) and displays comparable isotopic composition (Figure 9). These observations indicate that the cataclasite matrix derived from the hanging wall carbonates. During this period of thrust sheet emplacement, fractures F3 developed. We interpret that the orientation of these fractures represents the far-field stress regime unaltered by faulting (Figure 13(c)). The calcite cement Cc3, precipitated in fractures F3, reflects the presence of formation fluids and the progressive increase in precipitation temperatures, up to ~117°C, which could indicate progressive burial during fault growth from calcite cement Cc1 to Cc3 [107].

Later, the thrust acted as a preferential pathway for fluids that only infiltrated in the hanging wall block (Figure 13(c)) as indicated by the presence of the same calcite cement (Cc4) along the thrust slip plane, in the fault core and within the crackle proto-breccia from the hanging wall. Thus, this observation corroborates the compartmentalization of the fluid system. As proposed in other settings where faults compartmentalize fluid flow between the footwall and hanging wall, the presence of veins without a preferred structural orientation (i.e., randomly oriented veins) is indicative of overpressured fluid migrating during deformation. Pressured fluids were likely expelled from Cretaceous carbonates due to sediment compaction during thrust sheet emplacement [77] (Figure 13(c)).

The interpreted evolution of the studied fault zone is similar to models already proposed in other extensional settings during upward propagation of normal faults deforming carbonate rocks [71, 80, 89, 105, 108, 109]. Therefore, the comparison between these studies allows us to provide insights into deformation processes and mechanisms related to propagation of faults in different geological settings. Interestingly, all these contributions reported an initial stage of fault nucleation related to the development of a process zone (in the fault tip) before individualization of the fault plane. This period was characterized by the formation of hydraulic extension fracturing and brecciation and the presence of a fluid in chemical equilibrium with the host rocks. Finally, the progressive deformation resulted in the propagation of the fault (slip plane) through the process zone and the circulation of external fluids along the main slip surfaces (i.e.,

longitudinal fluid migration). These studies also reported an evolution of the fracture connectivity, a continuous opening of the fluid regime, and a progressive change in the fluid composition and origin during the evolution of the fault zone [80, 89, 105].

5.5. Structural Permeability: Thrust Sealing Capability and Fluid Pressuring. The petrology and geochemistry of the studied calcite cements indicate that the thrust separates two compartments with different deformation and fluid flow patterns. It is therefore likely that the thrust acted as a transversal barrier for fluids migrating between the footwall and hanging wall. The barrier role of the thrust is attributed (i) to the poor permeability of the foliated cataclasite and its micritic carbonate matrix with concentration of clay minerals associated with pressure-solution surfaces and (ii) to the nonporous character of the hanging wall carbonates (i.e., wackestones). In the latter case, although it has not been measured, the permeability is likely lower in the hanging wall wackestones with respect to the footwall grainstones. Therefore, the thrust acted as a transversal barrier and a longitudinal drain from fluids [15].

Additionally, considering the footwall damage zone as a high fractured compartment, its structural permeability is qualitatively evaluated. In this compartment, systematically oriented fractures (F1 to F3) were cemented by three generations of calcite cement (Cc1 to Cc3) and the randomly oriented fractures were cemented by Cc1 and Cc2. This evidences that the structural permeability was transient and that successive episodes of fracturing added new pathways to fluids that were rapidly occluded by calcite precipitation and sealing [18, 70]. According to theoretical models, the presence of existing fractures appropriately oriented for reactivation prevents the formation of new fracturing events [10]. Therefore, a new fracturing episode developed when the previous fracture system regained cohesive strength by calcite precipitation [10]. The fact that the calcite cements Cc1 to Cc3 vary geochemically through time demonstrate that the fluid pathways, path lengths (associated with different fracture sizes), and the extent of fluid-rock interaction changed during the thrust nucleation (process zone development) and growth (thrust slip plane propagation), which has been corroborated by the different fluid compositions and temperatures obtained from clumped isotopes. In the same location, a previous study [42] documented the distribution of fractures developed in the footwall and discussed the permeability properties of the footwall damage zone in terms of porosity creation and occluding processes based on structural analysis and crosscutting relationships between veins. These authors also concluded that the footwall damage zone had to be considered as a low-quality reservoir analogue because any porosity developed during fracturing was rapidly sealed by cementation processes [42].

The comparison between the above described scenario and the model proposed in the Oman Mountains [26] highlights that fluid behavior during thrusting greatly varies in different geological settings. In particular, the analysis of calcite cements precipitated across the fault zone in both studies reveals that the thrust faults acted as transversal barriers to fluid migration but were preferential paths for channelized fluids along the thrust planes (longitudinal drains). In the studied outcrop, fluids in the footwall did not reach the hanging wall because of the impermeable fault core rock (foliated cataclasite) and a different fluid migrated upwards along the thrust plane and towards the hanging wall. By contrast, in the outcrop of Oman [26], fluids migrated along the thrust fault and towards the footwall, the only block in which syntectonic fractures developed. Our contribution and that of [26] highlight the importance of a good understanding of the timing of fracturing and the associated fluids in order to characterize the hydraulic behavior of a fault zone.

6. Conclusions

The studied thrust displaces a subvertical Upper Cretaceous carbonate succession located in the southern limb of the Sant Corneli-Bóixols anticline, in the Southern Pyrenees. Structural data together with petrological and geochemical analyses of synkinematic calcite veins developed within the fault zone constrain the evolution of the structural permeability and the thrust sealing capability and provide insights into the paleofluid system at the time of thrusting:

(i) The heterogeneous distribution of deformation mechanisms across the thrust zone resulted in strong host rock dissolution within the fault core and calcite precipitation in veins within the damage zone

(ii) The evolution of the thrust zone resulted from the upward propagation of the fault tip, producing distributed deformation in the process zone and subsequent propagation of the fault (slip plane), similar to the models already proposed for normal faults deforming carbonate rocks. During this evolution, the different deformation and fluid flow histories in the footwall and hanging wall indicate that the fault core acted as a transversal barrier due to its low permeability associated with the foliated cataclasite arrangement and matrix cementation. In the footwall, three systematically oriented fracture systems (F1 to F3) and randomly oriented fractures developed during progressive deformation. The structural permeability in the footwall damage zone was transient, and successive episodes of fracturing added new pathways to fluids but were rapidly occluded by calcite precipitation. By contrast, in the hanging wall, only randomly oriented fractures are present

(iii) Three calcite cements (Cc1 to Cc3) precipitated within the fracture systems developed in the footwall. The petrology and geochemistry of Cc1 to Cc3 reveal a progressive change in the fluid origin and/or composition from percolation of meteoric fluids at temperatures between 42 and 51°C to upward migration of hotter formation waters at temperatures between 105 and 117°C. On the other hand, only one calcite cement (Cc4) precipitated in the hanging wall and in the fault core from hot

formation waters at 95°C. These formation fluids were probably expelled from Cretaceous carbonates and migrated along the thrust plane towards the hanging wall during deformation. The comparison between the present study and previous data reported in the eastern part of the Sant Corneli-Bóixols anticline reveals the same fluid regimen and evolution of the fluid system during the post-folding stages of deformation in the whole anticline

Data Availability

All data used to support the findings of this study are included within the article.

Conflicts of Interest

The authors declare that there is no conflict of interest regarding the publication of this paper.

Acknowledgments

This research was carried out within the framework of the Dirección General de Investigación Científica y Técnica Spanish Project (PGC2018-093903-B-C22) (Ministerio de Ciencia, Innovación y Universidades/Agencia Estatal de Investigación/Fondo Europeo de Desarrollo Regional, Unión Europea) and the Grup Consolidat de Recerca "Geologia Sedimentària" (2017-SGR-824). The PhD research of DM-L is supported by the FPI2016 (BES-2016-077214) Spanish program from MINECO.

References

[1] H. Watkins, D. Healy, C. E. Bond, and R. W. H. Butler, "Implications of heterogeneous fracture distribution on reservoir quality; an analogue from the Torridon Group sandstone, Moine Thrust Belt, NW Scotland," *Journal of Structural Geology*, vol. 108, pp. 180–197, 2018.

[2] J. W. Cosgrove, "The association of folds and fractures and the link between folding, fracturing and fluid flow during the evolution of a fold–thrust belt: a brief review," *Geological Society, London, Special Publications*, vol. 421, no. 1, pp. 41–68, 2015.

[3] A. Travé, P. Labaume, and J. Vergés, "Fluid systems in foreland fold-and-thrust belts: an overview from the Southern Pyrenees," in *Thrust Belts and Foreland Basins*, O. Lacombe, F. Roure, J. Lavé, and J. Vergés, Eds., pp. 93–115, Frontiers in Earth Sciences; Springer Berlin Heidelberg, Berlin, Heidelberg, 2007.

[4] E. Fitz-Diaz, P. Hudleston, L. Siebenaller et al., "Insights into fluid flow and water-rock interaction during deformation of carbonate sequences in the Mexican fold-thrust belt," *Journal of Structural Geology*, vol. 33, no. 8, pp. 1237–1253, 2011.

[5] J. Oliver, "Fluids expelled tectonically from orogenic belts: their role in hydrocarbon migration and other geologic phenomena," *Geology*, vol. 14, no. 2, p. 99, 1986.

[6] P. Muchez and M. Sintubin, "Contrasting origin of palaeofluids in a strike-slip fault system," *Chemical Geology*, vol. 145, no. 1-2, pp. 105–114, 1998.

[7] A. Gudmundsson, "Fluid overpressure and flow in fault zones: field measurements and models," *Tectonophysics*, vol. 336, no. 1-4, pp. 183–197, 2001.

[8] A. Gudmundsson, S. S. Berg, K. B. Lyslo, and E. Skurtveit, "Fracture networks and fluid transport in active fault zones," *Journal of Structural Geology*, vol. 23, no. 2-3, pp. 343–353, 2001.

[9] R. Sibson, "Frictional mechanics of seismogenic thrust systems in the upper continental crust—implications for fluid overpressures and redistribution," *Thrust Tectonics and Hydrocarbon Systems*, vol. 82, pp. 1–17, 2004.

[10] R. H. Sibson, "Tensile overpressure compartments on low-angle thrust faults," *Earth, Planets and Space*, vol. 69, no. 1, p. 113, 2017.

[11] R. H. Sibson, "Crustal stress, faulting and fluid flow," *Geological Society, London, Special Publications*, vol. 78, no. 1, pp. 69–84, 1994.

[12] C. Hilgers, D. L. Kirschner, J.-P. Breton, and J. L. Urai, "Fracture sealing and fluid overpressures in limestones of the Jabal Akhdar dome, Oman mountains," *Geofluids*, vol. 6, no. 2, pp. 168–184, 2006.

[13] R. Sibson and J. Scott, "Stress/fault controls on the containment and release of overpressured fluids: examples from gold-quartz vein systems in Juneau, Alaska; Victoria, Australia and Otago, New Zealand," *Ore Geology Reviews*, vol. 13, no. 1-5, pp. 293–306, 1998.

[14] R. H. Sibson, "Arterial faults and their role in mineralizing systems," *Geoscience Frontiers*, vol. 10, no. 6, pp. 2093–2100, 2019.

[15] J. S. Caine, J. P. Evans, and C. B. Forster, "Fault zone architecture and permeability structure," *Geology*, vol. 24, no. 11, p. 1025, 1996.

[16] S. J. Jolley, D. Barr, J. J. Walsh, and R. J. Knipe, "Structurally complex reservoirs: an introduction," *Geological Society, London, Special Publications*, vol. 292, no. 1, pp. 1–24, 2007.

[17] F. Agosta, M. Alessandroni, M. Antonellini, E. Tondi, and M. Giorgioni, "From fractures to flow: a field-based quantitative analysis of an outcropping carbonate reservoir," *Tectonophysics*, vol. 490, no. 3-4, pp. 197–213, 2010.

[18] F. Agosta, M. Prasad, and A. Aydin, "Physical properties of carbonate fault rocks, fucino basin (Central Italy): implications for fault seal in platform carbonates," *Geofluids*, vol. 7, no. 1, pp. 19–32, 2007.

[19] S. Barker, *Dynamics of fluid flow and fluid chemistry during crustal shortening*, vol. 250, pp. 331–344, 2007.

[20] A. Taillefer, R. Soliva, L. Guillou-Frottier, E. Le Goff, G. Martin, and M. Seranne, "Fault-related controls on upward hydrothermal flow: an integrated geological study of the Têt fault system, Eastern Pyrénées (France)," *Geofluids*, vol. 2017, 19 pages, 2017.

[21] A. Travé, P. Labaume, F. Calvet, and A. Soler, "Sediment dewatering and pore fluid migration along thrust faults in a foreland basin inferred from isotopic and elemental geochemical analyses (Eocene southern Pyrenees, Spain)," *Tectonophysics*, vol. 282, no. 1-4, pp. 375–398, 1997.

[22] B. Lacroix, L. P. Baumgartner, A.-S. Bouvier, P. D. Kempton, and T. Vennemann, "Multi fluid-flow record during episodic mode I opening: a microstructural and SIMS study (Cotiella thrust fault, Pyrenees)," *Earth and Planetary Science Letters*, vol. 503, pp. 37–46, 2018.

[23] V. Trincal, M. Buatier, D. Charpentier et al., "Fluid–rock interactions related to metamorphic reducing fluid flow in meta-sediments: example of the Pic-de-Port-Vieux thrust (Pyrenees, Spain)," *Contributions to Mineralogy and Petrology*, vol. 172, no. 9, p. 78, 2017.

[24] A. Travé, P. Labaume, F. Calvet et al., "Fluid migration during Eocene thrust emplacement in the south Pyrenean foreland basin (Spain): an integrated structural, mineralogical and geochemical approach," *Geological Society, London, Special Publications*, vol. 134, no. 1, pp. 163–188, 1998.

[25] L. F. Martinez Casas, A. Travé, D. Cruset, and D. Muñoz-López, "The Montagut fault system: geometry and fluid flow analysis (Southern Pyrennes, Spain)," *Petrogenesis and Exploration of the Earth's Interior*, pp. 211–214, 2019.

[26] L. Breesch, R. Swennen, and B. Vincent, "Fluid flow reconstruction in hanging and footwall carbonates: compartmentalization by Cenozoic reverse faulting in the Northern Oman Mountains (UAE)," *Marine and Petroleum Geology*, vol. 26, no. 1, pp. 113–128, 2009.

[27] I. Moretti, P. Labaume, S. M. F. Sheppard, and J. Boulègue, "Compartmentalisation of fluid migration pathways in the sub-Andean Zone, Bolivia," *Tectonophysics*, vol. 348, no. 1-3, pp. 5–24, 2002.

[28] P. Choukroune, "The Ecors Pyrenean deep seismic profile reflection data and the overall structure of an orogenic belt," *Tectonics*, vol. 8, no. 1, pp. 23–39, 1989.

[29] S. P. Srivastava, H. Schouten, W. R. Roest et al., "Iberian plate kinematics: a jumping plate boundary between Eurasia and Africa," *Nature*, vol. 344, no. 6268, pp. 756–759, 1990.

[30] J. A. Muñoz, "Evolution of a continental collision belt: ECORS-Pyrenees crustal balanced cross-section," in *Thrust Tectonics*, pp. 235–246, Springer Netherlands, Dordrecht, 1992.

[31] J. Vergés and M. Fernàndez, "Tethys–Atlantic interaction along the Iberia–Africa plate boundary: the Betic–Rif orogenic system," *Tectonophysics*, vol. 579, pp. 144–172, 2012.

[32] J. A. Muñoz, "Fault-related folds in the southern Pyrenees," *American Association of Petroleum Geologists Bulletin*, vol. 101, no. 4, pp. 579–587, 2017.

[33] J. A. Muñoz, A. Martinez, and J. Verges, "Thrust sequences in the eastern Spanish Pyrenees," *Journal of Structural Geology*, vol. 8, no. 3-4, pp. 399–405, 1986.

[34] M. Seguret and M. Daignieres, "Crustal scale balanced cross-sections of the Pyrenees; discussion," *Tectonophysics*, vol. 129, no. 1-4, pp. 303–318, 1986.

[35] F. Roure, P. Choukroune, X. Berastegui et al., "Ecors deep seismic data and balanced cross sections: geometric constraints on the evolution of the Pyrenees," *Tectonics*, vol. 8, no. 1, pp. 41–50, 1989.

[36] J. Verges and J. A. Munoz, "Thrust sequence in the southern central Pyrenees," *Bulletin de la Société Géologique de France*, vol. VI, no. 2, pp. 265–271, 1990.

[37] R. M. G. Bond and K. R. McClay, "Inversion of a Lower Cretaceous extensional basin, south central Pyrenees, Spain," *Geological Society, London, Special Publications*, vol. 88, no. 1, pp. 415–431, 1995.

[38] J. Mencos, "Metodologies de reconstrucció i modelització 3D d'estructures geològiques: anticlinal de Sant Corneli-Bóixols (Pirineus centrals)," *Universitat de Barcelona*, 2010, PhD thesis.

[39] S. Tavani, J. Mencos, J. Bausà, and J. A. Muñoz, "The fracture pattern of the Sant Corneli Bóixols oblique inversion anticline (Spanish Pyrenees)," *Journal of Structural Geology*, vol. 33, no. 11, pp. 1662–1680, 2011.

[40] J. M. Garcia-Senz, *Cuencas Extensivas del Cretácico Inferior en los Pirineos Centrales, formación y subsecuente inversión. PhD Thesis*, Universitat de Barcelona, Barcelona, 2002.

[41] J. Mencos, N. Carrera, and J. A. Muñoz, "Influence of rift basin geometry on the subsequent postrift sedimentation and basin inversion: the Organyà Basin and the Bóixols thrust sheet (south central Pyrenees)," *Tectonics*, vol. 34, no. 7, pp. 1452–1474, 2015.

[42] J. Gutmanis, L. Ardèvol i Oró, D. Díez-Canseco, L. Chebbihi, A. Awdal, and A. Cook, "Fracture analysis of outcrop analogues to support modelling of the subseismic domain in carbonate reservoirs, south-central Pyrenees," *Geological Society, London, Special Publications*, vol. 459, no. 1, pp. 139–156, 2018.

[43] J. Gallemí Paulet, R. Martínez Ribas, and J. Pons, *Unidades del Cretácico superior en los alrededores de San Corneli (Provincia de Lleida)*, Cuadernos de Geología Ibérica, Madrid, Spain, 1982.

[44] P. H. W. Mey, P. J. C. Nagtegaal, K. J. Roberti, and J. J. A. Hartevelt, "Lithostratigraphic subdivision of post-Hercynian deposits in the South-Central Pyrenees," *Leidse geologische mededelingen*, vol. 41, pp. 221–228, 1968.

[45] J. M. McCrea, "On the isotopic chemistry of carbonates and a paleotemperature scale," *The Journal of Chemical Physics*, vol. 18, no. 6, pp. 849–857, 1950.

[46] C. M. John and D. Bowen, "Community software for challenging isotope analysis: first applications of 'Easotope' to clumped isotopes," *Rapid Communications in Mass Spectrometry*, vol. 30, no. 21, pp. 2285–2300, 2016.

[47] W. Guo, J. L. Mosenfelder, W. A. Goddard, and J. M. Eiler, "Isotopic fractionations associated with phosphoric acid digestion of carbonate minerals: insights from first-principles theoretical modeling and clumped isotope measurements," *Geochimica et Cosmochimica Acta*, vol. 73, no. 24, pp. 7203–7225, 2009.

[48] K. W. Huntington, J. M. Eiler, H. P. Affek et al., "Methods and limitations of "clumped" CO_2 isotope (Δ_{47}) analysis by gas-source isotope ratio mass spectrometry," *Journal of Mass Spectrometry*, vol. 44, no. 9, pp. 1318–1329, 2009.

[49] K. J. Dennis, H. P. Affek, B. H. Passey, D. P. Schrag, and J. M. Eiler, "Defining an absolute reference frame for 'clumped' isotope studies of CO_2," *Geochimica et Cosmochimica Acta*, vol. 75, no. 22, pp. 7117–7131, 2011.

[50] S.-T. Kim and J. R. O'Neil, "Equilibrium and nonequilibrium oxygen isotope effects in synthetic carbonates," *Geochimica et Cosmochimica Acta*, vol. 61, no. 16, pp. 3461–3475, 1997.

[51] T. Kluge, C. M. John, A.-L. Jourdan, S. Davis, and J. Crawshaw, "Laboratory calibration of the calcium carbonate clumped isotope thermometer in the 25–250 °C temperature range," *Geochimica et Cosmochimica Acta*, vol. 157, pp. 213–227, 2015.

[52] N. H. Woodcock and K. Mort, "Classification of fault breccias and related fault rocks," *Geological Magazine*, vol. 145, no. 3, pp. 435–440, 2008.

[53] J. Veizer, D. Ala, K. Azmy et al., "87Sr/86Sr, δ13C and δ18O evolution of Phanerozoic seawater," *Chemical Geology*, vol. 161, no. 1-3, pp. 59–88, 1999.

[54] C. Delle Piane, M. B. Clennell, J. V. A. Keller, A. Giwelli, and V. Luzin, "Carbonate hosted fault rocks: a review of structural and microstructural characteristic with implications for seismicity in the upper crust," *Journal of Structural Geology*, vol. 103, pp. 17–36, 2017.

[55] G. S. Lister and A. W. Snoke, "S-C mylonites," *Journal of Structural Geology*, vol. 6, no. 6, pp. 617–638, 1984.

[56] J. M. McArthur and R. J. Howarth, "Shields, G.A. Strontium isotope stratigraphy," in *The Geologic Time Scale*, vol. 1–2, pp. 127–144, Elsevier, 2012.

[57] W. L. McIntire, "Trace element partition coefficients-a review of theory and applications to geology," *Geochimica et Cosmochimica Acta*, vol. 27, no. 12, pp. 1209–1264, 1963.

[58] A. Mucci and J. W. Morse, "The incorporation of Mg^{2+} and Sr^{2+} into calcite overgrowths: influences of growth rate and solution composition," *Geochimica et Cosmochimica Acta*, vol. 47, no. 2, pp. 217–233, 1983.

[59] A. Katz, "The interaction of magnesium with calcite during crystal growth at 25-90°C and one atmosphere," *Geochimica et Cosmochimica Acta*, vol. 37, no. 6, pp. 1563–1586, 1973.

[60] A. Katz, E. Sass, A. Starinsky, and H. D. Holland, "Strontium behavior in the aragonite-calcite transformation: an experimental study at 40-98°C," *Geochimica et Cosmochimica Acta*, vol. 36, no. 4, pp. 481–496, 1972.

[61] D. J. J. Kinsman, "Interpretation of Sr^{+2} concentrations in carbonate minerals and rocks," *SEPM Journal of Sedimentary Research*, vol. Vol. 39, 1969.

[62] M. Bau and P. Dulski, "Distribution of yttrium and rare-earth elements in the Penge and Kuruman iron-formations, Transvaal Supergroup, South Africa," *Precambrian Research*, vol. 79, no. 1-2, pp. 37–55, 1996.

[63] G. E. Webb and B. S. Kamber, "Rare earth elements in Holocene reefal microbialites: a new shallow seawater proxy," *Geochimica et Cosmochimica Acta*, vol. 64, no. 9, pp. 1557–1565, 2000.

[64] F. Salvini, A. Billi, and D. U. Wise, "Strike-slip fault-propagation cleavage in carbonate rocks: the Mattinata fault zone, southern Apennines, Italy," *Journal of Structural Geology*, vol. 21, no. 12, pp. 1731–1749, 1999.

[65] B. Lacroix, A. Travé, M. Buatier, P. Labaume, T. Vennemann, and M. Dubois, "Syntectonic fluid-flow along thrust faults: example of the south-Pyrenean fold-and-thrust belt," *Marine and Petroleum Geology*, vol. 49, pp. 84–98, 2014.

[66] P. D. Bons, M. A. Elburg, and E. Gomez-Rivas, "A review of the formation of tectonic veins and their microstructures," *Journal of Structural Geology*, vol. 43, pp. 33–62, 2012.

[67] K. Bitzer, A. Travé, and J. M. Carmona, "Fluid flow processes at basin scale," *Acta Geologica Hispánica*, vol. 36, pp. 1–20, 2001.

[68] R. H. Sibson, "Brittle-failure controls on maximum sustainable overpressure in different tectonic regimes," *American Association of Petroleum Geologists Bulletin*, vol. 87, no. 6, pp. 901–908, 2003.

[69] D. M. Saffer and H. J. Tobin, "Hydrogeology and mechanics of subduction zone forearcs: fluid flow and pore pressure," *Annual Review of Earth and Planetary Sciences*, vol. 39, no. 1, pp. 157–186, 2011.

[70] V. F. Bense, T. Gleeson, S. E. Loveless, O. Bour, and J. Scibek, "Fault zone hydrogeology," *Earth-Science Reviews*, vol. 127, pp. 171–192, 2013.

[71] J. M. Vermilye and C. H. Scholz, "The process zone: a microstructural view of fault growth," *Journal of Geophysical Research - Solid Earth*, vol. 103, no. B6, pp. 12223–12237, 1998.

[72] P. Upton, M. Begbie, and D. Craw, "Numerical modelling of mechanical controls on coeval steep and shallow dipping auriferous quartz vein formation in a thrust zone, Macraes mine, New Zealand," *Mineralium Deposita*, vol. 43, no. 1, pp. 23–35, 2008.

[73] M. J. Begbie and D. Craw, "Geometry and petrography of stockwork vein swarms, macraes mine, Otago schist, New Zealand," *New Zealand Journal of Geology and Geophysics*, vol. 49, no. 1, pp. 63–73, 2006.

[74] R. L. Enlow and P. O. Koons, "Critical wedges in three dimensions: analytical expressions from Mohr-Coulomb constrained perturbation analysis," *Journal of Geophysical Research - Solid Earth*, vol. 103, no. B3, pp. 4897–4914, 1998.

[75] J. J. Wilkinson and J. D. Johnston, "Pressure fluctuations, phase separation, and gold precipitation during seismic fracture propagation," *Geology*, vol. 24, no. 5, pp. 395–398, 1996.

[76] C. H. Scholz, N. H. Dawers, J.-Z. Yu, M. H. Anders, and P. A. Cowie, "Fault growth and fault scaling laws: preliminary results," *Journal of Geophysical Research - Solid Earth*, vol. 98, no. B12, pp. 21951–21961, 1993.

[77] B. Dewever, R. Swennen, and L. Breesch, "Fluid flow compartmentalization in the Sicilian fold and thrust belt: implications for the regional aqueous fluid flow and oil migration history," *Tectonophysics*, vol. 591, pp. 194–209, 2013.

[78] Y. Branquet, A. Cheilletz, G. Giuliani, B. Laumonier, and O. Blanco, "Fluidized hydrothermal breccia in dilatant faults during thrusting: the Colombian emerald deposits," *Geological Society, London, Special Publications*, vol. 155, no. 1, pp. 183–195, 1999.

[79] S. F. J. Cox, M. A. Knackstedt, and J. W. Braun, "Principles of structural control on permeability and fluid flow in hydrothermal systems," *Structural Controls on Ore Genesis; Society of Economic Geologists*, pp. 1–24, 2001.

[80] M. Bussolotto, A. Benedicto, L. Moen-Maurel, and C. Invernizzi, "Fault deformation mechanisms and fault rocks in micritic limestones: examples from Corinth rift normal faults," *Journal of Structural Geology*, vol. 77, pp. 191–212, 2015.

[81] R. H. Sibson, "Structural permeability of fluid-driven fault-fracture meshes," *Journal of Structural Geology*, vol. 18, no. 8, pp. 1031–1042, 1996.

[82] P. Labaume, S. Sheppard, and I. Moretti, "Structure and hydraulic behaviour of cataclastic thrust fault zones in sandstones, Sub-Andean Zone, Bolivia," *Journal of Geochemical Exploration*, vol. 69-70, pp. 487–492, 2000.

[83] I. Moretti, P. Labaume, S. Sheppard, and J. Boulegue, "Compartmentalisation of fluid flow by thrust faults, Sub-Andean Zone, Bolivia," *Journal of Geochemical Exploration*, vol. 69–70, pp. 493–497, 2000.

[84] R. Tostevin, G. A. Shields, G. M. Tarbuck, T. He, M. O. Clarkson, and R. A. Wood, "Effective use of cerium anomalies as a redox proxy in carbonate-dominated marine settings," *Chemical Geology*, vol. 438, pp. 146–162, 2016.

[85] H. Irwin, C. Curtis, and M. Coleman, "Isotopic evidence for source of diagenetic carbonates formed during burial of organic-rich sediments," *Nature*, vol. 269, no. 5625, pp. 209–213, 1977.

[86] T. E. Cerling, J. Quade, Y. Wang, and J. R. Bowman, "Carbon isotopes in soils and palaeosols as ecology and palaeoecology indicators," *Nature*, vol. 341, no. 6238, pp. 138-139, 1989.

[87] M. R. Howson, A. D. Pethybridge, and W. A. House, "Synthesis and distribution coefficient of low-magnesium calcites," *Chemical Geology*, vol. 64, no. 1-2, pp. 79–87, 1987.

[88] I. Cantarero, A. Travé, G. Alías, and V. Baqués, "Pedogenic products sealing normal faults (Barcelona Plain, NE Spain)," *Journal of Geochemical Exploration*, vol. 106, no. 1-3, pp. 44–52, 2010.

[89] V. Baqués, A. Travé, A. Benedicto, P. Labaume, and I. Cantarero, "Relationships between carbonate fault rocks and fluid flow regime during propagation of the Neogene extensional faults of the Penedès basin (Catalan Coastal Ranges, NE Spain)," *Journal of Geochemical Exploration*, vol. 106, no. 1-3, pp. 24–33, 2010.

[90] S. Boggs and D. Krinsley, *Application of Cathodoluminescence Imaging to the Study of Sedimentary Rocks*, Cambridge University Press, Cambridge, UK, 2006.

[91] V. Vandeginste, R. Swennen, M. Allaeys, R. M. Ellam, K. Osadetz, and F. Roure, "Challenges of structural diagenesis in foreland fold-and-thrust belts: a case study on paleofluid flow in the Canadian Rocky Mountains West of Calgary," *Marine and Petroleum Geology*, vol. 35, no. 1, pp. 235–251, 2012.

[92] N. Beaudoin, N. Bellahsen, O. Lacombe, and L. Emmanuel, "Fracture-controlled paleohydrogeology in a basement-cored, fault-related fold: Sheep Mountain Anticline, Wyoming, United States," *Geochemistry, Geophysics, Geosystems*, vol. 12, no. 6, 2011.

[93] H. G. Machel, "Application of cathodoluminescence to carbonate diagenesis," in *Cathodoluminescence in Geosciences*, pp. 271–301, Springer Berlin Heidelberg, Berlin, Heidelberg, 2000.

[94] R. Worden, "Quantitative diagenesis: recent developments and applications to reservoir geology," *Marine and Petroleum Geology*, vol. 13, no. 5, pp. 597-598, 1996.

[95] A. Travé, F. Calvet, M. Sans, J. Vergés, and M. Thirlwall, "Fluid history related to the Alpine compression at the margin of the south-Pyrenean foreland basin: the El Guix anticline," *Tectonophysics*, vol. 321, no. 1, pp. 73–102, 2000.

[96] I. P. Montañez and L. J. Crossey, "Diagenesis," in *Encyclopedia of Geochemistry*, W. M. White, Ed., Encyclopedia of Earth Sciences Series; Springer International Publishing, Cham, 2017.

[97] P. Nuriel, G. Rosenbaum, J.-X. Zhao et al., "U-Th dating of striated fault planes," *Geology*, vol. 40, no. 7, pp. 647–650, 2012.

[98] N. Vilasi, R. Swennen, and F. Roure, "Diagenesis and fracturing of Paleocene-Eocene carbonate turbidite systems in the Ionian Basin: the example of the Kelçyra area (Albania)," *Journal of Geochemical Exploration*, vol. 89, no. 1-3, pp. 409–413, 2006.

[99] L. Lefticariu, E. C. Perry, M. P. Fischer, and J. L. Banner, "Evolution of fluid compartmentalization in a detachment fold complex," *Geology*, vol. 33, no. 1, p. 69, 2005.

[100] M. P. Fischer, I. C. Higuera-Díaz, M. A. Evans, E. C. Perry, and L. Lefticariu, "Fracture-controlled paleohydrology in a map-scale detachment fold: insights from the analysis of fluid inclusions in calcite and quartz veins," *Journal of Structural Geology*, vol. 31, no. 12, pp. 1490–1510, 2009.

[101] M. A. Evans, G. E. Bebout, and C. H. Brown, "Changing fluid conditions during folding: an example from the Central Appalachians," *Tectonophysics*, vol. 576-577, pp. 99–115, 2012.

[102] D. Cruset, I. Cantarero, J. Vergés, C. M. John, D. Muñoz-López, and A. Travé, "Changes in fluid regime in syn-orogenic sediments during the growth of the south Pyrenean fold and thrust belt," *Global and Planetary Change*, vol. 171, pp. 207–224, 2018.

[103] N. Nardini, D. Muñoz-López, D. Cruset et al., "From early contraction to post-folding fluid evolution in the frontal part of the Bóixols thrust sheet (Southern Pyrenees) as revealed by the texture and geochemistry of calcite cements," *Minerals*, vol. 9, no. 2, p. 117, 2019.

[104] O. Oms, V. Fondevilla, V. Riera et al., "Transitional environments of the lower Maastrichtian South-Pyrenean Basin (Catalonia, Spain): the Fumanya member tidal flat," *Cretaceous Research*, vol. 57, pp. 428–442, 2016.

[105] P. Labaume, E. Carrio-Schaffhauser, J.-F. Gamond, and F. Renard, "Deformation mechanisms and fluid-driven mass transfers in the recent fault zones of the Corinth Rift (Greece)," *Comptes Rendus Geoscience*, vol. 336, no. 4-5, pp. 375–383, 2004.

[106] Z. Reches and D. A. Lockner, "Nucleation and growth of faults in brittle rocks," *Journal of Geophysical Research-Solid Earth*, vol. 99, no. B9, pp. 18159–18173, 1994.

[107] F. X. Passelègue, O. Fabbri, M. Dubois, and S. Ventalon, "Fluid overpressure along an Oligocene out-of-sequence thrust in the Shimanto Belt, SW Japan," *Journal of Asian Earth Sciences*, vol. 86, pp. 12–24, 2014.

[108] I. S. Stewart and P. L. Hancock, "Brecciation and fracturing within neotectonic normal fault zones in the Aegean region," *Geological Society, London, Special Publications*, vol. 54, no. 1, pp. 105–110, 1990.

[109] I. S. Stewart and P. L. Hancock, "Normal fault zone evolution and fault scarp degradation in the Aegean region," *Basin Research*, vol. 1, pp. 139–153, 1988.